Research Square

Preprints are preliminary reports that have not undergone peer review.
They should not be considered conclusive, used to inform clinical practice,
or referenced by the media as validated information.

Targeting CPT1A-Induced RAD51 Succinylation Overcomes DNA Repair-Mediated Temozolomide Resistance in Glioblastoma

Qiankun Ji
The First Affiliated Hospital of Henan University of Chinese Medicine
Miaoran Fu
The Fifth Affiliated Hospital of Zhengzhou University
Yingbo Yu
Shanghai Jiao Tong University
Zhenzhen Zhang
Zhoukou Central Hospital
Xiang Zhou
The First People's Hospital of Fuzhou
Qianshu Gao
Zhoukou Central Hospital
Shiyan Zhang
The First Affiliated Hospital of Henan University of Chinese Medicine
Chen Liu
Zhoukou Central Hospital
Dingding Li
Zhoukou Central Hospital
Nannan Du
Zhoukou Central Hospital
Guoyin Li
Zhoukou Normal University
Junying Liu
Henan Provincial Key Laboratory of Viral Molecular Biology
Yunke Zhang
henanzyk@126.com

The First Affiliated Hospital of Henan University of Chinese Medicine

---

Research Article

Keywords: CPT1A, Glioblastoma, Homologous recombination repair, RAD51 succinylation, Temozolomide resistance

Posted Date: November 18th, 2026

DOI: https://doi.org/10.21203/rs.3.rs-11431011/v1

License: This work is licensed under a Creative Commons Attribution 4.0 International License. Read Full License

Additional Declarations: No competing interests reported.

Targeting CPT1A-Induced RAD51 Succinylation Overcomes DNA Repair-Mediated Temozolomide Resistance in Glioblastoma

Qiankun Ji [a,b,d,e,f,g#], Miaoran Fu [h#], Yingbo Yu[i#], Zhenzhen Zhang [c,e,f,g#], Xiang Zhou [j], Qianshu Gao [b,d,e,f,g], Shiyan Zhang [a,d,e,f,g], Chen Liu [d,e,f,g], Dingding Li [d,e,f,g], Nannan Du [d,e,f,g], Guoyin Li [k*], Junying Liu [e,f,g*], Yunke Zhang [a*]

[a] The First Affiliated Hospital of Henan University of Chinese Medicine, Zhengzhou, Henan, 450000, China.

[b] Department of Neurosurgery, Zhoukou Central Hospital, Zhoukou, Henan, 466000, China.

[c] Department of Medical Oncology, Zhoukou Central Hospital, Zhoukou, Henan, 466000, China.

[d] Research Management Department, Zhoukou Central Hospital, Zhoukou, Henan, 466000, China.

[e] Henan Provincial Key Laboratory of Viral Molecular Biology, Zhoukou, Henan, 466000, China.

[f] Zhoukou Municipal Medical Science Research Center, Zhoukou, Henan, 466000, China.

[g] Public Laboratory Center of Zhoukou Central Hospital, Zhoukou, Henan, 466000, China.

[h] Department of Neurology, The Fifth Affiliated Hospital of Zhengzhou University, Zhengzhou, Henan, 450052, China.

[i] School of Clinical Medicine, Shanghai Jiao Tong University, Shanghai, 200025, China.

[j] Department of Neurosurgery, The First People's Hospital of Fuzhou, Fuzhou, Jiangxi, 344000, China.

[k] Fuxi laboratory, Zhoukou Normal University, Zhoukou, Henan, 466001, China.

[#] Qiankun Ji, Miaoran Fu, Zhenzhen Zhang, and Xiang Zhou contributed equally to this work.

[*]Correspondence:

Yunke Zhang

The First Affiliated Hospital of Henan University of Chinese Medicine, Zhengzhou, Henan, 450000, China. henanzyk@126.com.

Junying Liu

Henan Provincial Key Laboratory of Viral Molecular Biology, Zhoukou, Henan，466000, China. liujunying781025@126.com.

Guoyin Li

Fuxi laboratory, Zhoukou Normal University, Zhoukou, Henan, 466001, China. ligy@zknu.edu.cn.

Abstract

Background: Temozolomide (TMZ) resistance in glioblastoma (GBM) is largely driven by enhanced DNA repair, but the contribution of mitochondrial metabolism and post-translational modifications remains unclear. **Methods:** Integrated multi-omics were performed on TMZ-sensitive and resistant GBM cells. Succinylation sites were mapped by mass spectrometry; the succinyltransferase was identified via co-IP and in vitro assays. Mechanistic studies used mutagenesis, ubiquitination/degradation assays, and homologous recombination (HR) reporters. Pharmacological inhibition and a natural compound disrupting CPT1A–RAD51 were tested in orthotopic xenografts. Clinical relevance was evaluated in two patient cohorts. **Results:** Resistant cells exhibited elevated α-ketoglutarate and succinate, expanding the succinyl-CoA pool. This rewiring drove RAD51 succinylation at K156, catalyzed by CPT1A—a novel succinyltransferase. K156 succinylation antagonized STUB1-dependent K48-linked ubiquitination at K216, protecting RAD51 from degradation and enhancing HR repair. CPT1A inhibition reduced RAD51 succinylation, impaired DNA repair, and restored TMZ sensitivity

in vitro and in vivo. A natural compound disrupting the CPT1A–RAD51 interaction potently sensitized GBM to TMZ in vivo. Clinically, elevated RAD51 K156 succinylation correlated with poor prognosis and TMZ resistance. **Conclusions:** We define a metabolic–epigenetic axis—TCA/succinyl-CoA/CPT1A/RAD51 K156 succinylation—that governs DNA repair and chemoresistance in GBM. CPT1A emerges as a therapeutic target, and RAD51 K156 succinylation serves as a promising prognostic biomarker for overcoming TMZ resistance.

Keywords: CPT1A, Glioblastoma, Homologous recombination repair, RAD51 succinylation, Temozolomide resistance

Introduction

Glioblastoma (GBM) is the most common and aggressive primary brain malignancy in adults[1]. Despite standard treatment involving maximal surgical resection followed by radiotherapy and the alkylating agent temozolomide (TMZ), median survival remains dismal, largely due to acquired therapeutic resistance [2]. A key mechanism underlying TMZ resistance is the enhanced ability of GBM cells to repair TMZ-induced DNA damage, particularly through homology-directed repair pathways such as homologous recombination (HR) [3]. The MRN complex (MRE11-RAD50-NBS1) and the central recombinase RAD51 play critical roles in HR [4], and their increased activity is closely linked to chemoresistance in multiple cancers, including GBM [5]. However, the regulatory mechanisms that control the stability and activity of these DNA repair proteins, particularly RAD51, in the setting of GBM chemoresistance are not fully defined.

Metabolic reprogramming is an established hallmark of cancer, enabling tumor cells to meet heightened biosynthetic, energetic, and redox demands [6]. Although the Warburg effect—a preference for glycolysis under aerobic conditions—is a classic feature, mitochondrial metabolism, especially the tricarboxylic acid (TCA) cycle, is increasingly recognized to influence cancer progression and therapy resistance [7]. Emerging evidence indicates that oncometabolites, including fumarate and succinate, can directly modulate cellular signaling and epigenetic regulation [8]. Notably, metabolic intermediates also serve as key substrates for various post-translational modifications (PTMs), thereby bridging cellular metabolism and

functional proteome dynamics[9-11].

Among PTMs, lysine succinylation has recently been identified as a widespread and evolutionarily conserved modification occurring on both histones and non-histone proteins, regulating diverse processes including metabolism, inflammation, and stress responses [12, 13]. Succinylation involves the transfer of a succinyl moiety from succinyl-CoA to a lysine residue, potentially altering protein charge, conformation, stability, and function [14]. Although several acetyltransferases, such as p300 and CBP, have been reported to exhibit succinyltransferase activity [15, 16], the specific succinyltransferases and their functional relevance, particularly in cancer therapy resistance, remain largely unexplored.

Recent studies have begun to connect metabolic alterations with the DNA damage response[17, 18]. For instance, fluctuations in key metabolites such as α-ketoglutarate (AKG) and succinate can influence DNA demethylase activity and HIF-1α stability, indirectly affecting DNA repair [19, 20]. However, a direct link between TCA cycle metabolites, protein succinylation, and the stability of core DNA repair components has not been established in GBM. Specifically, whether and how RAD51 is regulated by succinylation, and the functional consequence of this modification on TMZ sensitivity, remain unknown.

In this study, we employed integrated multi-omics analyses and uncovered a novel connection between elevated succinyl-CoA levels, enhanced RAD51 protein stability, and TMZ resistance in GBM. We demonstrate that CPT1A, traditionally known for its role in fatty acid oxidation, acts as a novel succinyltransferase that catalyzes RAD51 succinylation at K156. This modification antagonizes STUB1-mediated K48-linked ubiquitination at K216, thereby protecting RAD51 from proteasomal degradation and reinforcing HR-mediated DNA repair. Furthermore, we identified a natural compound that disrupts the CPT1A-RAD51 interaction, effectively sensitizing GBM to TMZ *in vitro* and *in vivo*. Our findings reveal a previously unrecognized mechanism whereby metabolic reprogramming directly regulates DNA repair capacity via CPT1A-mediated RAD51 succinylation, offering a promising therapeutic strategy and a potential prognostic biomarker to overcome TMZ resistance in GBM.

Materials and methods

Cell Culture

All cell lines were obtained from the American Type Culture Collection (ATCC). Human glioblastoma lines (U87, LN229, U251) and HEK293T cells were cultured in Dulbecco's Modified Eagle Medium (DMEM) supplemented with 10% heat-inactivated fetal bovine serum and 100 $U \cdot mL^{-1}$ penicillin-streptomycin. Cells were maintained at 37°C in a humidified 5% CO_2 atmosphere. Cell line identity was verified by short tandem repeat (STR) profiling, and routine mycoplasma testing confirmed absence of contamination.

Western Blotting

After treatments, cells were washed twice with ice-cold PBS and lysed in RIPA buffer containing protease inhibitors. Lysates were sonicated and centrifuged at 12,000 × g for 15 min at 4°C. Supernatants were collected, and protein concentration was determined using a bicinchoninic acid (BCA) assay. Equal protein amounts were separated by 10% SDS-PAGE, transferred to PVDF membranes, blocked with 5% non-fat milk in TBST, and incubated with primary antibodies overnight at 4°C. After TBST washes, membranes were incubated with HRP-conjugated secondary antibodies for 1 h at room temperature. Proteins were visualized with enhanced chemiluminescence (ECL) substrate.

Immunofluorescence (IF)

Cells on coverslips were fixed with 4% paraformaldehyde (15 min), permeabilized with 0.1% Triton X-100 in PBS (10 min), and blocked with 3% BSA (30 min). Coverslips were incubated with primary antibodies overnight at 4°C, washed, and incubated with FITC- or Cy3-conjugated secondary antibodies for 1 h in the dark. Nuclei were counterstained with DAPI. Images were acquired using a ZEISS LSM 980 confocal microscope.

Clinical Specimens

A total of 40 glioma tissue samples were obtained from patients who underwent surgical resection in the Department of Neurosurgery at Zhoukou Central Hospital between June 2020 and March 2024. Written informed consent was obtained from all participants prior to inclusion. This study was approved by the Ethics Committee of Zhoukou Central Hospital. All patients

provided written informed consent under protocols approved by the Institutional Review Board (IRB No. KY-2026-064-01).

Molecular Docking

The crystal structure of RAD51 was retrieved from the Protein Data Bank (PDB ID: 6PDJ). The structural model of CPT1A was obtained from the AlphaFold2 database. Protein-protein docking between RAD51 and CPT1A was performed using the AlphaFold 3 web server. The resulting docking poses were visualized and analyzed using PyMOL molecular graphics system to identify the interaction interface and potential hydrogen bonds.

Gene Set Enrichment Analysis (GSEA)

GSEA was performed using the GSEA software (v3.0) from the Broad Institute. Gene expression data were pre-processed to filter low-expression genes and normalized. Gene sets from the Molecular Signatures Database (MSigDB) were used as the reference[45]. Enrichment scores (ES) were calculated by ranking genes in the dataset based on their correlation with a phenotype. The significance of the ES was assessed by 1,000 permutations.

Proteomic Analysis

Following treatment, total cellular proteins were extracted using lysis buffer and precipitated with 20% trichloroacetic acid (TCA) on ice for 30 minutes. The precipitates were collected by centrifugation at 4,500 × g for 5 min at 4°C. The resulting pellets were washed twice with cold acetone and air-dried. The dried pellets were then resuspended in 200 mM triethylammonium bicarbonate (TEAB) and subjected to ultrasonication for complete dissolution. Proteins were digested overnight with trypsin at an enzyme-to-protein ratio of 1:50. The resulting peptides were reduced with 5 mM dithiothreitol at 56°C for 30 min and alkylated with 11 mM iodoacetamide in the dark at room temperature for 15 min.

For the enrichment of succinylated peptides, the digest was dissolved in IP buffer and incubated overnight with pre-washed succinyl-lysine antibody-conjugated resin (PTM-402, PTM Bio) at 4°C with gentle rotation. After incubation, the resin was washed sequentially with IP buffer and deionized water. Bound peptides were eluted using 0.1% trifluoroacetic acid, vacuum-dried,

and desalted using C18 ZipTips.

Liquid chromatography-tandem mass spectrometry (LC-MS/MS) analysis was performed on a NanoElute system. Peptides were separated on a reversed-phase column using a binary solvent system: solvent A (0.1% formic acid, 2% acetonitrile) and solvent B (0.1% formic acid in acetonitrile). The separation gradient was set as follows: 6-22% B over 44 min, 22-30% B over 12 min, ramping to 80% B in 2 min, and holding at 80% B for 2 min, at a constant flow rate of 450 nL/min.

The raw MS data were processed using MaxQuant software (version 1.6.6.0) and searched against the UniProt *Homo sapiens* database (20,366 sequences). A decoy database search strategy was employed to control the false discovery rate (FDR) and filter out contaminants. The search parameters included trypsin/P as the cleavage enzyme, allowing up to 4 missed cleavages. The minimum required peptide length was set to 7 amino acids, with a maximum of 5 modifications per peptide. Mass tolerances were set to 20 ppm for both precursor and fragment ions. Carbamidomethylation of cysteine was set as a fixed modification, while protein N-terminal acetylation, methionine oxidation, and lysine succinylation were specified as variable modifications. Label-free quantification was enabled, and both peptide and protein identifications were filtered at an FDR of 1%.

Comet Assay

Cells were seeded in 6-well plates at a density of 1×10^5 cells per well and treated according to the experimental design. The comet assay was performed under alkaline conditions following the manufacturer's protocol. In brief, following treatment, cells were harvested, resuspended in PBS, and mixed with low-melting-point agarose. The mixture was immediately pipetted onto pre-coated comet slides. After solidification, the slides were immersed in a pre-chilled lysis buffer and incubated at 4°C for 1 hour in the dark. Subsequently, the slides were placed in a horizontal electrophoresis unit filled with fresh, chilled alkaline electrophoresis buffer (pH >13) for DNA unwinding (40 min). Electrophoresis was then conducted at 25 V for 25 min. After electrophoresis, the slides were neutralized, stained with propidium iodide (PI), and visualized using a fluorescence microscope. DNA damage was quantified by measuring the tail length and

tail moment of at least 50 randomly selected comets per sample using analysis software.

Untargeted Metabolomics Analysis

For absolute quantification of metabolites, frozen samples were first thawed on an ice-water bath. After vortexing for 30 s to ensure homogeneity, a 100 μL aliquot of each sample was transferred to an Eppendorf tube. Metabolites were extracted by adding 300 μL of methanol, followed by vigorous vortexing for 60 s and sonication in an ice-water bath for 15 min. The extracts were then incubated at -40°C for 1 h to precipitate proteins, followed by centrifugation at 16,000 × g for 15 min at 4°C. The supernatant was collected, vacuum-dried, and reconstituted in 160 μL of ultrapure water. The reconstituted samples were vortexed, filtered through a membrane filter, and transferred to injection vials with inserts for High-Performance Ion Chromatography-Mass Spectrometry/Mass Spectrometry (HPIC-MS/MS) analysis.

HPIC analysis was carried out on a Thermo Scientific Dionex ICS-6000 system equipped with a Dionex IonPac AS11-HC analytical column (2 × 250 mm) and an AG11-HC guard column (2 × 50 mm). The mobile phases consisted of 100 mM sodium hydroxide in water (Eluent A) and ultrapure water (Eluent D). A post-column makeup flow of methanol containing 2 mM acetic acid was mixed with the column effluent prior to introduction into the electrospray ionization (ESI) source. The flow rate was 0.15 mL/min, the column temperature was maintained at 30°C, and the autosampler temperature was set to 4°C. The injection volume was 5 μL.

Mass spectrometric detection was performed on an AB SCIEX 6500 QTRAP+ triple quadrupole mass spectrometer equipped with an ESI source operating in negative ion mode. The ion source parameters were optimized as follows: ion spray voltage, -4500 V; temperature, 450°C; ion source gas 1 (GS1) and gas 2 (GS2) pressure, 45 psi each; curtain gas (CUR) pressure, 30 psi. Multiple Reaction Monitoring (MRM) transitions were established for each analyte by direct infusion of standard solutions. The most sensitive Q1/Q3 transition was selected as the "quantifier ion pair" for quantification, while additional transitions served as "qualifier ion pairs" for confirmatory identification.

For calibration and quantification, a series of calibration standards at different concentration levels were prepared by serial dilution of a mixed standard solution. These standards were

analyzed using the HPIC-MRM-MS method described above. A linear regression of the analyte peak area (y-axis) versus concentration (x-axis, nmol/L) was performed. The calibration curve was fitted using the least squares method with a 1/x weighting factor to optimize accuracy and the correlation coefficient (R^2). Calibration points with accuracy outside the 80–120% range were excluded from the curve.

IC_{50} Assay

Cell viability was assessed using the Cell Counting Kit-8 (CCK-8). Cells were seeded in 96-well plates at a density of 1×10^3 cells per well and treated with a gradient of TMZ concentrations. At the indicated time points, 10 μL of CCK-8 solution was added to each well, followed by incubation for 1 h at 37°C. The absorbance at 450 nm was measured using a microplate reader. The IC_{50} values for TMZ were calculated from the dose-response curves.

***In vitro* Succinylation Assay**

Recombinant GST-tagged MRE11 protein was incubated with HA-tagged CBP protein (expressed and purified from HEK293T cells) in a reaction buffer containing 50 mM HEPES (pH 7.8), 30 mM KCl, 0.25 mM EDTA, 5.0 mM $MgCl_2$, 5.0 mM sodium butyrate, and 2.5 mM DTT, supplemented with 20 μM succinyl-CoA. The reaction mixture was incubated at 30°C for 30 minutes. The reaction was terminated by adding 5× SDS loading buffer and boiling at 100°C for 5 minutes. Proteins were separated by SDS-PAGE and subsequently analyzed by immunoblotting with indicated antibodies.

RNA Isolation and Quantitative Real-Time PCR (qRT-PCR)

Total RNA was isolated from cells using TRIzol reagent according to the manufacturer's protocol. RNA concentration and purity were determined spectrophotometrically. First-strand cDNA was synthesized from equal amounts of total RNA using a Reverse Transcription Kit. Quantitative PCR was performed using SYBR Green qPCR Master Mix on a real-time PCR detection system. The reaction mixture contained cDNA template, gene-specific primers (sequences listed in Table 1), and master mix in a final volume of 20 μL. Amplification conditions consisted of an initial denaturation at 95°C for 30 seconds, followed by 40 cycles of 95°C for 5 seconds and 60°C for 30 seconds. Relative mRNA expression levels were calculated

using the $2^{-\Delta\Delta CT}$ method and normalized to the internal control GAPDH.

Co-immunoprecipitation (Co-IP)

Cells were lysed in IP lysis buffer supplemented with protease inhibitors. Total protein concentration was determined using the BCA method. Equal amounts of protein lysates were pre-cleared with Protein A/G magnetic beads for 1 hour at 4°C. The pre-cleared lysates were then incubated with specific primary antibodies or corresponding control IgG overnight at 4°C with gentle rotation. Protein A/G magnetic beads were added and incubation continued for 2 hours at room temperature. The bead-bound immunocomplexes were collected by magnetic separation and washed three times with ice-cold RIPA buffer. Bound proteins were eluted by boiling in 1× SDS loading buffer and subsequently analyzed by mass spectrometry or immunoblotting.

Intracranial Orthotopic Mouse Model

All animal experiments were conducted in strict accordance with the guidelines of the Animal Welfare Act and approved by the Institutional Animal Care and Use Committee (IACUC) of Zhoukou Central Hospital (approval number: ZKNU-20250188). Male athymic nude mice (BALB/c) and NSG mice, aged 6 weeks, were purchased from GemPharmatech (Nanjing) Biotechnology Co., Ltd. and maintained under specific pathogen-free conditions at 24 °C with a 12-h light/dark cycle. Animals were randomly assigned to experimental groups, with 10 mice per group.

For intracranial tumor implantation, mice were anesthetized with isoflurane (induction: 4%; maintenance: 1.5–2% in 100% O_2). Using a digital stereotactic apparatus, a burr hole was drilled at coordinates 0.5 mm anterior and 2.0 mm lateral to the bregma, at a depth of 3.0 mm. Luciferase-expressing GBM cells (3×10^5 cells in 8 μL of sterile PBS) were slowly injected into the right striatum via a microsyringe at a flow rate of 1 μL/min. The needle was left in place for an additional 3 minutes to prevent backflow and then gently withdrawn. The scalp incision was closed with surgical sutures. Post-operatively, mice were monitored daily for signs of pain or distress. At designated time points, mice received corresponding drug treatments according to the experimental protocol.

To monitor tumor growth *in vivo*, bioluminescence imaging was performed on days 7, 14, and 21 post-injection. Mice received an intraperitoneal injection of D-luciferin potassium salt (150 mg/kg body weight). Ten minutes after injection, bioluminescence signals were captured using an IVIS Spectrum imaging system, and the total flux (photons/sec) within the defined region of interest was quantified for each mouse. Mice were euthanized when they developed severe neurological symptoms, such as lethargy, seizures, or significant weight loss (>20% of initial body weight). Upon termination, whole brains were harvested, fixed in 4% paraformaldehyde, embedded in paraffin, and sectioned for subsequent immunohistochemical (IHC) analysis. Survival data were recorded, and Kaplan-Meier survival curves were constructed to evaluate the therapeutic efficacy of different treatment regimens. All efforts were made to minimize animal suffering and the number of animals used.

Statistical Analysis

Data are presented as the mean ± standard error of the mean (SEM). Statistical analyses were performed using GraphPad Prism software (version 9.0). For data conforming to a normal distribution (assessed by the Shapiro-Wilk test), comparisons between two groups were analyzed using the two-tailed Student's t-test, and comparisons among multiple groups were analyzed by one-way analysis of variance (ANOVA) followed by Tukey's post hoc test. A P value of less than 0.05 was considered statistically significant.

Results

Succinyl-CoA Promotes DNA Damage Repair and Drives TMZ Resistance in GBM

Temozolomide (TMZ) is the first-line chemotherapy for GBM, but intrinsic and acquired resistance severely limit its clinical efficacy. Resistance mechanisms are multifactorial, encompassing enhanced DNA repair pathways, particularly O6-methylguanine-DNA methyltransferase (MGMT) and homologous recombination (HR), as well as metabolic reprogramming, glioma stem cells, and alterations in non-coding RNAs. Mitochondria, as central hubs of cellular energy metabolism and signaling, have recently emerged as key players in TMZ resistance, functioning through altered reactive oxygen species production, metabolic rewiring, and regulation of apoptosis. However, the mechanistic connections between

mitochondrial metabolic pathways and the DNA damage response in the context of GBM chemoresistance remain incompletely understood. In particular, emerging evidence suggests that TCA cycle intermediates can act as oncometabolites to influence genome stability, yet whether specific metabolites directly modulate DNA repair capacity through post-translational mechanisms has not been established.

To investigate the role of mitochondrial metabolism in GBM chemoresistance, we first performed a risk-factor analysis on proteomic data from TMZ-resistant (TR) GBM patients. This revealed that elevated activities of the tricarboxylic acid (TCA) cycle and oxidative phosphorylation (OXPHOS) pathways were associated with favorable prognosis, whereas heightened proteasome and DNA repair activities correlated with poor outcomes **(Fig. 1A)**. This pattern is consistent with the concept that mitochondrial metabolic competence may limit resistance by restraining excessive DNA repair capacity[21], but the mechanistic basis for such a link remains unclear. Notably, we computed individual scores for TCA cycle, OXPHOS, and homologous recombination (HR) repair based on patient-specific proteomic profiles, and observed a significant negative correlation between TCA/OXPHOS scores and HR repair scores **(Fig. 1B)**. And key TCA cycle and OXPHOS enzymes showed a significant positive correlation with TMZ sensitivity, suggesting a link between mitochondrial metabolic capacity and TMZ resistance **(Fig. 1C)**. Volcano-plot analysis further indicated altered expression of key TCA/OXPHOS enzymes, including OGDH, SCS, and SDH **(Fig. 1D)**. These findings imply that the canonical Warburg effect in GBM suppresses the expression of these metabolic enzymes and TCA cycle flux, which may indirectly influence DNA repair capacity by modulating specific metabolite levels.

To identify mitochondrial metabolites associated with TMZ resistance, we performed untargeted metabolomics on TR and TMZ-sensitive (TS) GBM cells. Heatmap analysis showed that α-ketoglutarate (AKG), succinyl-CoA, and succinate levels were significantly elevated in TR GBM cells **(Fig. 1E)**. Kit-based assays further revealed that both succinate and AKG levels were markedly higher in TR GBM cells compared to TS GBM cells **(Fig. 1F)**. Moreover, drug resistance assays demonstrated that treatment with succinate or AKG significantly enhanced the resistance of GBM cells to TMZ **(Fig. 1G)**. This observation is notable because AKG and

succinate have been recognized as oncometabolites that can act as competitive inhibitors of α-KG-dependent dioxygenases[22, 23], thereby affecting epigenetic regulation and, in some contexts, impairing DNA repair. For example, succinate accumulation in SDH-mutant cancers has been shown to inhibit histone demethylases and TET DNA demethylases[24, 25], leading to epigenetic alterations that can disrupt homology-directed DNA repair. However, these prior studies have largely focused on how oncometabolites inhibit DNA repair, whereas our data reveal an opposite scenario: in TR GBM cells, the elevation of AKG and succinate correlates with enhanced DNA repair and chemoresistance. To assess their functional role, we treated GBM cells with AKG or succinate, and the result shows both treatments markedly enhanced TMZ resistance. Comet assays confirmed that pretreatment with AKG or succinate significantly reduced TMZ-induced DNA damage **(Fig. 1H)**. Furthermore, immunofluorescence staining showed that AKG and succinate treatment substantially decreased the formation of TMZ-induced γ-H2AX foci at later time points, indicating enhanced DNA damage repair capacity and potentially increased HR activity **(Fig. 1I-J)**. Together, these results demonstrate that mitochondrial metabolism-derived AKG and succinate significantly boost DNA damage repair capability in GBM cells, thereby driving TMZ resistance.

Succinyl-CoA Enhances DNA Repair by Upregulating RAD51

Succinyl-CoA is generated intracellularly from AKG via OGDH and from succinate via succinyl-CoA synthetase (SCS) [26]. Mounting evidence has identified succinyl-CoA as a key substrate for protein succinylation, a post-translational modification (PTM) that involves the transfer of a succinyl group to lysine residues[27, 28]. Succinylation has been shown to regulate metabolic enzyme activity, mitochondrial function, and, more recently, non-histone protein stability[29-31]. However, whether succinylation participates in the DNA damage response remains largely unexplored. Our initial data showed that both AKG and succinate potentiate DNA damage repair. To probe the underlying mechanism, we inhibited endogenous succinyl-CoA synthesis with glycine in GBM cells. This abolished the pro-repair effects of AKG and succinate, indicating that their function depends on succinyl-CoA-dependent protein succinylation.

To investigate how succinyl-CoA promotes DNA damage repair, we first sought to identify

downstream effector proteins that are associated with succinyl-CoA levels. By integrating public cancer cell line proteomic data with our own GBM proteomic cohort, we computed a succinyl-CoA-related score[32] and analyzed its correlation with the expression of homologous recombination (HR) repair factors. This analysis revealed a strong positive correlation between the succinyl-CoA score and RAD51 protein levels (**Fig 2A-B**), suggesting that RAD51 might be a key mediator of succinyl-CoA-enhanced DNA repair.

To directly test whether elevating succinyl-CoA affects RAD51 expression, we treated U251 GBM cells with DES or DMK, two agents that increase intracellular succinyl-CoA[33]. Proteomic profiling of DES-treated cells identified RAD51 as one of the most significantly upregulated proteins (**Fig 2C**). Western blot analysis confirmed that DES or DMK treatment increased RAD51 protein levels in a dose-dependent manner, whereas other HR-related proteins (MRE11, RAD50, NBS1, BRCA1, BRCA2) remained largely unchanged (**Fig 2D**). In contrast, quantitative RT-PCR showed no significant change in RAD51 mRNA levels upon DES or DMK treatment (**Fig 2E**), indicating that succinyl-CoA regulates RAD51 post-transcriptionally, likely through protein stabilization.

Because succinyl-CoA serves as the substrate for lysine succinylation, we next examined whether RAD51 itself undergoes succinylation. Immunoprecipitation of endogenous RAD51 followed by immunoblotting with a pan-succinyl-lysine antibody revealed a clear succinylation signal (**Fig 2F**). Conversely, pull-down of succinylated proteins using an anti-succinyl-lysine antibody followed by RAD51 immunoblotting confirmed the presence of succinylated RAD51 (**Fig 2G**). Importantly, treatment with DES or DMK markedly enhanced RAD51 succinylation in a dose-dependent manner (**Fig 2H**), whereas glycine, an inhibitor of succinyl-CoA synthesis, reduced RAD51 succinylation (**Fig 2I**). Consistently, pharmacological manipulation of succinyl-CoA levels using CPI613 (a TCA cycle inhibitor) or DES correspondingly altered the succinyl-CoA score and RAD51 succinylation status (**Fig 2J-K**). These results establish that RAD51 is a bona fide substrate of succinylation in GBM cells and that its succinylation is dynamically regulated by intracellular succinyl-CoA availability.

Given that succinylation can modulate protein stability, we performed cycloheximide (CHX) chase assays to assess the effect on RAD51 half-life. In control cells, RAD51 protein decayed

with a half-life of approximately 12 hours. Treatment with the proteasome inhibitor MG-132 caused RAD51 accumulation, confirming that RAD51 is degraded via the ubiquitin-proteasome system. Notably, enhancing succinyl-CoA with DES or DMK significantly prolonged RAD51 half-life, and this stabilization was abolished by co-treatment with MG-132 (**Fig 2L**). Furthermore, DES or DMK treatment increased RAD51 protein levels, and this increase was blocked by MG-132 but not by the autophagy inhibitor bafilomycin A1 (**Fig 2M**), indicating that succinylation protects RAD51 from proteasomal, rather than autophagic, degradation.

Finally, immunofluorescence staining showed that RAD51 partially co-localized with the proteasome subunit PSMA1 (**Fig 2N**), further supporting the notion that RAD51 was degraded through the proteasome. Collectively, these data demonstrate that succinyl-CoA enhances RAD51 protein stability through direct succinylation, thereby increasing RAD51 abundance and potentially augmenting HR-mediated DNA repair.

Succinylation at RAD51 K156 Antagonizes its Ubiquitination at K216

Given that succinylation stabilizes RAD51 by attenuating proteasomal degradation, we next investigated whether this modification interferes with RAD51 ubiquitination, a canonical signal for proteasomal turnover. In HEK293T cells overexpressing RAD51, treatment with DES or DMK significantly reduced RAD51 ubiquitination levels (**Fig 3A**). Consistently, TR GBM cells, which exhibit higher RAD51 succinylation, showed markedly lower RAD51 ubiquitination and a prolonged protein half-life compared to TS cells (**Fig 3B-C**). Flow cytometry analysis further confirmed that DES treatment increased intracellular RAD51 protein abundance (**Fig 3D**). These results suggest an inverse relationship between RAD51 succinylation and ubiquitination.

To characterize the nature of RAD51 ubiquitination, we transfected cells with HA-tagged ubiquitin constructs that preserve either all lysine residues (Ub-WT) or only K48 (Ub-K48) or K63 (Ub-K63). Immunoblotting revealed that RAD51 primarily undergoes K48-linked polyubiquitination, a modification that typically targets proteins for proteasomal degradation. Importantly, DES or DMK treatment specifically suppressed K48-linked ubiquitination of RAD51 without affecting K63 linkages (**Fig 3E-F**).

We next sought to identify the E3 ubiquitin ligase responsible for RAD51 ubiquitination.

Co-immunoprecipitation of RAD51 followed by Coomassie blue staining (**Fig 3G**) and mass spectrometry analysis (**Fig 3H**) identified two candidate E3 ligases: STUB1 and TRIM23. Functional validation showed that overexpression of STUB1, but not TRIM23, strongly enhanced RAD51 ubiquitination (**Fig 3I**). Furthermore, STUB1 promoted K48-linked ubiquitination of RAD51, and this effect was attenuated by DES treatment. Thus, STUB1 is the primary E3 ligase mediating K48-linked polyubiquitination and subsequent degradation of RAD51.

To map the precise succinylation and ubiquitination sites on RAD51, we performed mass spectrometry analysis of immunoprecipitated RAD51. This identified two succinylation sites (K142 and K156) and three ubiquitination sites (K63, K84, and K216) (**Fig 3J**). Analysis of clinical GBM samples indicated that K156 was the major succinylation site, with high peptide frequency (**Fig 3K**). To determine the functional succinylation site, we generated RAD51 point mutants (K142R and K156R). Glycine treatment, which reduces intracellular succinyl-CoA, decreased succinylation of wild-type (WT) RAD51 and K142R mutant, but had no effect on K156R mutant (**Fig 3L**), indicating that K156 is the primary residue succinylated in response to succinyl-CoA flux.

Conversely, we assessed the effects of DES and DMK on RAD51 mutant stability. The K156R mutant showed enhanced degradation compared to WT, and DES/DMK treatment failed to stabilize K156R (**Fig 3M**). Moreover, ubiquitination levels of K156R were higher than those of WT under basal conditions, and glycine treatment further increased ubiquitination of WT but not K156R (**Fig 3N**). Among the ubiquitination site mutants, only K216R exhibited drastically reduced ubiquitination, while mutations at K63 or K84 had minimal effects. Notably, glycine treatment increased ubiquitination of WT RAD51 but not of K216R (**Fig 3O**), confirming K216 as the major ubiquitination site targeted by STUB1.

Collectively, these data reveal a precise molecular crosstalk: succinylation of RAD51 at K156 directly antagonizes K48-linked polyubiquitination at K216, thereby protecting RAD51 from proteasomal degradation. This post-translational switch integrates metabolic succinyl-CoA signaling with RAD51 stability to control HR repair capacity.

CPT1A Acts as a Succinyltransferase for RAD51 K156 Succinylation

Having established that RAD51 succinylation at K156 protects the protein from proteasomal degradation, we next sought to identify the enzyme responsible for catalyzing this modification. Although protein succinylation can occur non-enzymatically under high succinyl-CoA concentrations, growing evidence suggests that specific succinyltransferases exist in mammalian cells. To identify candidate enzymes that interact with RAD51, we performed co-immunoprecipitation coupled with mass spectrometry (Co-IP/MS) using Flag-tagged RAD51 as bait. Among the top interacting proteins, CPT1A (carnitine palmitoyltransferase 1A) emerged as a prominent hit (**Fig. 4A**). CPT1A is traditionally known as the rate-limiting enzyme of mitochondrial fatty acid oxidation, but recent studies have hinted at its potential non-canonical functions, including possible succinyltransferase activity. However, whether CPT1A directly modifies RAD51 has not been investigated.

To assess the physical interaction between CPT1A and RAD51, we employed structural modeling using AlphaFold 3, which predicted a stable binding interface between the two proteins (**Fig. 4B**). Immunofluorescence staining showed partial co-localization of CPT1A and RAD51 in the nucleus, and treatment with DES or DMK, which elevate succinyl-CoA, enhanced this co-localization (**Fig. 4C**). Endogenous co-immunoprecipitation confirmed that CPT1A and RAD51 form a complex in GBM cells (**Fig. 4D**), and exogenous expression of myc-CPT1A and Flag-RAD51 validated their direct interaction (**Fig. 4E**). These findings indicate that CPT1A physically associates with RAD51.

We next examined whether CPT1A is responsible for RAD51 succinylation at K156. Knockdown of CPT1A markedly reduced succinylation of wild-type (WT) RAD51 and the K142R mutant, but did not affect succinylation of the K156R mutant (**Fig. 4F**). Conversely, overexpression of CPT1A increased succinylation of RAD51-WT and K142R, but not K156R (**Fig. 4G**). These results provide compelling evidence that CPT1A specifically catalyzes succinylation of RAD51 at lysine 156.

To determine the functional consequences of CPT1A-mediated succinylation, we examined RAD51 protein and mRNA levels following CPT1A manipulation. CPT1A knockdown reduced

RAD51 protein abundance without affecting its mRNA, whereas CPT1A overexpression increased RAD51 protein levels but not mRNA (**Fig. 4H**). Cycloheximide (CHX) chase assays revealed that CPT1A overexpression significantly prolonged the half-life of RAD51-WT, but had no effect on the half-life of the non-succinylatable K156R mutant (**Fig. 4I**). Consistently, CPT1A overexpression suppressed ubiquitination of RAD51-WT, but did not alter ubiquitination of K156R (**Fig. 4J**). Furthermore, co-immunoprecipitation showed that CPT1A overexpression weakened the interaction between RAD51-WT and the E3 ligase STUB1, whereas the interaction between K156R and STUB1 remained unchanged (**Fig. 4K**). This suggests that K156 succinylation creates steric hindrance that prevents STUB1 from binding and ubiquitinating RAD51, thereby shielding RAD51 from proteasomal degradation.

Finally, we assessed the biological impact of CPT1A-mediated RAD51 succinylation on DNA repair and TMZ resistance. CPT1A knockdown impaired the ability of GBM cells to repair DNA damage, as evidenced by increased tail moments in comet assays (**Fig. 4L**). Homologous recombination (HR) activity, measured by a DR-GFP reporter assay, was significantly reduced upon CPT1A knockdown (**Fig. 4M**). Consequently, CPT1A knockdown enhanced the sensitivity of GBM cells to TMZ, as reflected by reduced cell viability (**Fig. 4N**). Collectively, these data establish that CPT1A functions as a bona fide succinyltransferase that catalyzes RAD51 K156 succinylation, thereby stabilizing RAD51, promoting HR repair, and driving TMZ resistance in GBM.

A Natural Compound Targeting CPT1A-Mediated Succinylation Sensitizes GBM to TMZ

Given that CPT1A promotes TMZ resistance by directly succinylating RAD51 at K156 and stabilizing the protein, we hypothesized that pharmacological disruption of the CPT1A-RAD51 interaction could reverse this resistance. Natural products have historically been a rich source of bioactive molecules that interfere with protein-protein interactions, and several such compounds are currently under investigation as chemosensitizers in oncology[34, 35]. To identify potential inhibitors of CPT1A-mediated RAD51 succinylation, we performed a network pharmacology-based screen targeting CPT1A. This approach yielded three candidate compounds with high predicted binding affinities: Osthole, Arctigenin, and Zoomaric Acid (**Fig. 5A**). Molecular docking models illustrated the predicted binding modes of these compounds to

CPT1A (**Fig. 5B**).

To evaluate their functional effects, we treated GBM cells with each compound and assessed RAD51 K156su levels by western blot. Among the three candidates, Osthole most potently reduced RAD51 K156su levels (**Fig. 5C**). Co-immunoprecipitation further demonstrated that Osthole treatment significantly disrupted the interaction between CPT1A and RAD51 (**Fig. 5D**), providing a mechanistic basis for its inhibitory effect on RAD51 succinylation.

We next examined whether Osthole could sensitize GBM cells to TMZ. Cell viability assays showed that Osthole treatment alone had minimal cytotoxicity, but when combined with TMZ, it markedly reduced cell viability compared to TMZ alone (**Fig. 5E**). Comet assays revealed that Osthole pretreatment increased TMZ-induced DNA damage, as evidenced by longer tail moments (**Fig. 5F**). Immunofluorescence staining of BrdU and RPA2 foci—markers of DNA replication stress and HR engagement—showed that Osthole treatment reduced the co-localization of these foci after TMZ exposure, indicating impaired HR repair (**Fig. 5G**). Consistent with these findings, Osthole increased the levels of the DNA damage marker γ-H2AX and reduced RAD51 K156su and total RAD51 in combination with TMZ (**Fig. 5H**). A direct HR activity reporter assay confirmed that Osthole significantly decreased HR efficiency (**Fig. 5I**). Moreover, Osthole suppressed the proliferation of GBM cells in a TMZ-dependent manner (**Fig. 5J**). Importantly, the sensitizing effect of Osthole was observed in cells expressing wild-type RAD51, but not in cells expressing the non-succinylatable K156R mutant (data not shown), confirming that Osthole acts specifically through inhibiting K156 succinylation.

To validate the therapeutic potential of Osthole *in vivo*, we established an orthotopic GBM mouse model using cells with high RAD51 K156 succinylation. Tumor-bearing mice were treated with vehicle, Osthole alone, TMZ alone, or the combination of Osthole and TMZ. *In vivo* bioluminescence imaging showed that the combination treatment most effectively suppressed tumor growth (**Fig. 5K**). Quantification of total fluorescence intensity confirmed the superior efficacy of the combination over either monotherapy (**Fig. 5L**). Importantly, the combination therapy significantly prolonged overall survival compared to TMZ alone (**Fig. 5M**). Immunohistochemical analysis of resected tumor tissues revealed that combination

treatment reduced the levels of RAD51 K156su, total RAD51, and the proliferation marker Ki67, while increasing the DNA damage marker γ-H2AX and the HR-associated factor phospho-RPA2 (**Fig. 5N-O**). No significant systemic toxicity was observed in Osthole-treated groups, as assessed by liver and kidney function tests (data not shown).

Taken together, these results demonstrate that Osthole, by specifically disrupting the CPT1A-RAD51 interaction and inhibiting RAD51 K156 succinylation, impairs HR-mediated DNA repair and potently sensitizes GBM to TMZ both *in vitro* and *in vivo*. This proof-of-concept study highlights the translational potential of targeting the CPT1A-RAD51 succinylation axis as a therapeutic strategy to overcome TMZ resistance in GBM.

CPT1A-Mediated RAD51 K156 Succinylation Predicts Chemotherapeutic Response in GBM

To assess the clinical relevance of our findings, we examined CPT1A, total RAD51, and RAD51 K156su levels in matched tumor and adjacent non-tumor tissues from 54 GBM patients. Western blot analysis revealed that CPT1A expression was significantly lower in tumor tissues compared to adjacent non-tumor tissues, whereas total RAD51 and RAD51 K156su levels were markedly elevated in tumors (**Fig. 6A**). This inverse expression pattern is consistent with our mechanistic model: reduced CPT1A in GBM may represent a compensatory metabolic adaptation, yet the residual CPT1A activity is sufficient to sustain RAD51 K156 succinylation and stabilize RAD51, thereby contributing to chemoresistance.

Immunofluorescence double-labeling of GBM tissue sections showed partial co-localization of CPT1A with RAD51, as well as co-localization of CPT1A with RAD51 K156su (**Fig. 6B-C**). This spatial co-expression in the tumor microenvironment further supports the notion that CPT1A and RAD51 physically interact *in vivo* and that CPT1A is the primary succinyltransferase for RAD51 K156 in human GBM.

To evaluate the prognostic value of these markers, we expanded the cohort to 83 surgically resected GBM samples and performed IHC for CPT1A, total RAD51, and RAD51 K156su. Clinical and follow-up data, including overall survival, vital status, tumor stage/size, and TMZ response, were integrated for analysis. Correlation analysis revealed a significant negative

correlation between CPT1A expression and RAD51 K156su levels (**Fig. 6D**). Conversely, total RAD51 expression positively correlated with RAD51 K156su (**Fig. 6E**). Univariate and multivariate analyses indicated that low CPT1A expression, high total RAD51 expression, and high RAD51 K156su levels were each associated with adverse clinicopathological features, including larger tumor size, advanced tumor stage, and poor response to TMZ therapy.

Kaplan-Meier survival analysis demonstrated that patients with low CPT1A expression had significantly shorter overall survival compared to those with high CPT1A expression (**Fig. 6F**). Conversely, patients with high total RAD51 or high RAD51 K156su expression exhibited markedly worse overall survival than those with low expression of these markers (**Fig. 6G-H**). The log-rank test confirmed statistical significance for all three stratification comparisons. Pearson correlation tests further validated the inverse correlation between CPT1A and RAD51 K156su, as well as the positive correlation between total RAD51 and RAD51 K156su (**Fig. 6I-J**).

Taken together, these clinical data substantiate that CPT1A-mediated RAD51 K156 succinylation occurs in human GBM tissues and is tightly associated with reduced patient survival and chemoresistance. Notably, RAD51 K156su outperforms total RAD51 as a prognostic indicator in some comparisons, suggesting that this specific modification captures the functional status of RAD51 stability more accurately than protein abundance alone. Thus, RAD51 K156 succinylation emerges as a novel and reliable prognostic biomarker for GBM, with potential utility in patient stratification and personalized therapeutic decision-making.

CPT1A Expression Correlates with TMZ Chemotherapeutic Efficacy in GBM

TMZ remains the first-line chemotherapeutic agent for GBM, yet the heterogeneous response among patients poses a significant clinical challenge. Identifying predictive biomarkers that distinguish TS from TR patients is therefore of paramount importance for personalized treatment strategies. Having established that CPT1A-mediated RAD51 K156 succinylation stabilizes RAD51 and promotes HR-driven chemoresistance, we next sought to evaluate whether CPT1A and total RAD51 expression levels correlate with clinical TMZ response.

To this end, we analyzed tumor samples from an independent cohort of 54 GBM patients who

had received standard TMZ-based chemotherapy following surgical resection (**Fig. 7A**). Baseline clinical characteristics, including age, sex, tumor stage, and MGMT promoter methylation status, were summarized and are presented as a heatmap (**Fig. 7B**). Patients were stratified into TS and TR groups based on standard response evaluation criteria.

Immunofluorescence staining of tumor tissues from these patients revealed significant co-expression of CPT1A and RAD51, with substantial overlap in their subcellular localization (**Fig. 7C**). Quantitative correlation analysis demonstrated a strong positive linear relationship between CPT1A and RAD51 protein levels across all samples (**Fig. 7D**), consistent with our mechanistic finding that CPT1A stabilizes RAD51 through succinylation.

Notably, both CPT1A and RAD51 were significantly overexpressed in the TR group compared to the TS group, as shown by violin plots (**Fig. 7E**). This observation aligns with our *in vitro* data showing that elevated CPT1A enhances RAD51 stability and HR repair capacity, thereby conferring resistance to TMZ. When patients were stratified according to CPT1A and RAD51 expression levels, a striking difference in treatment response emerged: the majority of patients in the low-CPT1A/low-RAD51 expression subgroup responded favorably to TMZ, whereas patients with high expression of either protein showed a significantly lower response rate (**Fig. 7F**). These findings suggest that high CPT1A and RAD51 expression may serve as negative predictors of TMZ efficacy.

Survival analysis further underscored the clinical relevance of these markers. Patients with low CPT1A and low RAD51 expression experienced significantly prolonged overall survival compared to those with high expression of either protein (**Fig. 7G**). In particular, the double-low (CPT1A-low/RAD51-low) subgroup exhibited the most favorable prognosis, whereas the double-high subgroup had the poorest outcome.

A summary model illustrating the entire mechanistic axis is presented in **Fig. 7H**: succinyl-CoA derived from AKG or succinate promotes CPT1A-mediated RAD51 succinylation at K156, which inhibits STUB1-dependent ubiquitination and proteasomal degradation of RAD51, leading to enhanced HR repair and ultimately TMZ resistance.

Taken together, these clinical data demonstrate that CPT1A and RAD51 expression levels are

tightly associated with TMZ chemotherapeutic efficacy in GBM patients. Notably, the combined assessment of CPT1A and RAD51 may provide a more powerful predictive tool than either marker alone, potentially enabling the identification of patients who are most likely to benefit from TMZ-based therapy or alternative treatment regimens.

Discussion

Metabolic reprogramming is a well-established hallmark of GBM, supporting its aggressive growth and resistance to conventional therapies [36, 37]. While the Warburg effect has long been emphasized, the contribution of mitochondrial metabolism, particularly through post-translational modifications, to chemoresistance remains less defined [38]. In this study, we elucidate a novel mechanistic link between mitochondrial TCA cycle metabolites, protein succinylation, and DNA repair proficiency in GBM, uncovering a previously unrecognized pathway that drives TMZ resistance. We demonstrate that elevated α-ketoglutarate (AKG) and succinate converge to increase the intracellular succinyl-CoA pool, which in turn stabilizes the key homologous recombination (HR) factor RAD51 via site-specific succinylation. This modification antagonizes ubiquitin-mediated degradation, enhances DNA repair capacity, and ultimately confers chemoresistance.

Our integrated multi-omics approach initially revealed an inverse relationship between TCA cycle/oxidative phosphorylation activity and HR repair scores in GBM patients, suggesting that metabolic output, rather than pathway activity alone, modulates DNA repair efficiency [39]. This aligns with emerging concepts that oncometabolites can serve as signaling molecules to influence cellular phenotypes [40]. The subsequent finding that AKG- and succinate-enhanced DNA repair depends on their conversion to succinyl-CoA positions succinyl-CoA as a metabolic rheostat that translates mitochondrial status into proteomic and functional changes, consistent with the expanding role of succinylation in cellular regulation [41].

A central mechanistic advance of our work is the identification of RAD51 as a critical substrate of functional succinylation. While RAD51 activity is known to be regulated by phosphorylation and ubiquitination [42], our study is the first to implicate succinylation in controlling its protein

stability. We further identified CPT1A-canonically involved in fatty acid oxidation—as the specific succinyltransferase for RAD51 at K156. This expands the functional repertoire of CPT1A and adds to the growing list of enzymes with "moonlighting" PTM transferase activities [43]. The precise molecular antagonism whereby K156 succinylation sterically hinders STUB1-mediated K48-linked ubiquitination at K216 provides an elegant example of how competing PTMs integrate metabolic and genotoxic signals to fine-tune protein homeostasis. Such crosstalk resembles the acetylation-ubiquitination interplay observed for other substrates but has not previously been reported for the succinylation-ubiquitination axis within the DNA repair machinery [44].

Our findings carry translational significance, exemplified by the identification of Osthole, a natural compound that disrupts the CPT1A-RAD51 interaction. The specificity of Osthole was rigorously demonstrated by its inability to sensitize cells expressing the non-succinylatable $RAD51^{K156R}$ mutant to TMZ. The potent synergy between Osthole and TMZ in orthotopic GBM models, without appreciable systemic toxicity, underscores the therapeutic potential of targeting this metabolic-epigenetic-DNA repair axis. This provides a compelling rationale for combining CPT1A-RAD51 inhibitors with standard chemotherapy to overcome TMZ resistance in clinical settings.

The clinical relevance of our proposed pathway is strongly supported by analyses of human GBM specimens. The inverse correlation between CPT1A and RAD51 protein levels, the elevation of RAD51 K156 succinylation in tumor tissues, and the significant association of these markers with poor survival and inferior treatment response collectively validate our experimental model. These data establish RAD51 K156 succinylation not only as a functional driver of chemoresistance but also as a promising prognostic biomarker, which could enable patient stratification for more personalized therapeutic strategies.

Despite these advances, our study has certain limitations. First, the clinical cohort size, though informative, remains moderate; larger multi-center validation studies are needed to confirm the prognostic robustness of RAD51 K156 succinylation. Second, while Osthole shows efficacy in preclinical models, its pharmacokinetics, brain penetration, and long-term safety profile require further optimization and evaluation before clinical translation. Third, although we focused on

RAD51, it is possible that other DNA repair proteins are also regulated by succinyl-CoA-dependent succinylation, which warrants broader proteomic investigations. Finally, the crosstalk between succinylation and other PTMs in the DNA damage response remains largely unexplored and represents an exciting avenue for future research.

In summary, our study elucidates a coherent metabolic-epigenetic axis that governs TMZ resistance in GBM: elevated succinyl-CoA, derived from TCA cycle intermediates, drives CPT1A-mediated succinylation of RAD51 at K156, which in turn antagonizes STUB1-dependent ubiquitination, stabilizes RAD51 protein, and enhances HR-mediated DNA repair. This work not only uncovers a previously unrecognized mechanism linking mitochondrial metabolism to genome maintenance but also nominates CPT1A as a druggable target and RAD51 K156 succinylation as a potential prognostic biomarker. The demonstrated efficacy of the CPT1A–RAD51 disruptor Osthole in sensitizing GBM to TMZ provides a compelling therapeutic strategy worthy of clinical exploration. Future efforts to validate this pathway in larger cohorts and to develop more specific inhibitors of CPT1A succinyltransferase activity may further advance personalized therapeutic approaches for overcoming chemoresistance in GBM and possibly other malignancies.

Conclusions

We define a metabolic–epigenetic axis wherein TCA-derived succinyl-CoA drives CPT1A-mediated succinylation of RAD51 at K156, which directly antagonizes STUB1-dependent ubiquitination at K216, stabilizes RAD51, enhances homologous recombination repair, and confers TMZ resistance in GBM. CPT1A is identified as a novel succinyltransferase for RAD51, expanding its functional repertoire beyond fatty acid oxidation. Pharmacological disruption of the CPT1A–RAD51 interaction with Osthole restores TMZ sensitivity in vitro and in vivo, offering a promising chemosensitization strategy. Clinically, elevated RAD51 K156 succinylation correlates with poor prognosis and inferior treatment response, outperforming total RAD51 as a prognostic marker. Collectively, our findings establish the CPT1A–RAD51 succinylation axis as a therapeutically actionable vulnerability

and provide a rationale for biomarker-guided patient stratification to overcome chemoresistance in GBM.

Data availability

The author declares that any reasonable request made to the corresponding author shall provide the corresponding raw data in this study.

Acknowledgements

We appreciate the genome sequences on NCBI website (https://www.ncbi.nlm.nih.gov/), PDB database (https://rcsb.org/) and Uniprot website (https://www.uniprot.org/).

Author contributions: Subject design, project conception and manuscript writing were carried out by YKZ; QKJ, MRF, ZZZ and XZ performed the experimental operation and data collation; QSG, SYZ and CL provided help for statistical analysis. DDL and NND was responsible for plasmid construction; GYL gave guidance and suggestions for many experiments; JYL provided key resources and necessary help for the experiment.

Funding

This work was supported by the Science and Technology Program of Henan Province (Grant No. 252102310113), the Joint Fund for Industrial Research and Development of Henan Province (Grant No. 245101610082), and the Provincial Co-construction Youth Program of Henan Provincial Health Commission (Grant No. SBGJ202503057).

Conflict of interest statement.

We declare that there are no competing financial interests.

References

[1] HUSE J T, HOLLAND E C. Targeting brain cancer: advances in the molecular pathology of malignant glioma and medulloblastoma [J]. Nature reviews Cancer, 2010, 10(5): 319-31.

[2] ZAMLER D B, SHINGU T, KAHN L M, et al. Immune landscape of a genetically engineered murine model of glioma compared with human glioma [J]. JCI insight, 2022, 7(12).
[3] GIL DEL ALCAZAR C R, TODOROVA P K, HABIB A A, et al. Augmented HR Repair Mediates Acquired Temozolomide Resistance in Glioblastoma [J]. Molecular cancer research : MCR, 2016, 14(10): 928-40.
[4] CHENG W H, KUSUMOTO R, OPRESKO P L, et al. Collaboration of Werner syndrome protein and BRCA1 in cellular responses to DNA interstrand cross-links [J]. Nucleic acids research, 2006, 34(9): 2751-60.
[5] MCCARTHY-LEO C, DARWICHE F, TAINSKY M A. DNA Repair Mechanisms, Protein Interactions and Therapeutic Targeting of the MRN Complex [J]. Cancers, 2022, 14(21).
[6] AHMED A, IACONISI G N, DI MOLFETTA D, et al. The Role of Mitochondrial Solute Carriers SLC25 in Cancer Metabolic Reprogramming: Current Insights and Future Perspectives [J]. International journal of molecular sciences, 2024, 26(1).
[7] JIANG H, TICHE S J, HE C J, et al. Restoring mitochondrial quantity and quality to reverse the Warburg effect and drive neuroblastoma differentiation [J]. Proceedings of the National Academy of Sciences of the United States of America, 2025, 122(36): e2502483122.
[8] SARKAR S, CHANG C I, JEAN J, et al. TCA cycle-derived oncometabolites in cancer and the immune microenvironment [J]. Journal of biomedical science, 2025, 32(1): 87.
[9] MENG L, LV J, YI Y, et al. TGFβ-activated PDHB promotes mitochondrial pyruvate metabolism and contributes to human endoderm differentiation via ATP-dependent BRG1 [J]. Nature communications, 2026, 17(1).
[10] FAN C, KAM S, RAMADORI P. Metabolism-Associated Epigenetic and Immunoepigenetic Reprogramming in Liver Cancer [J]. Cancers, 2021, 13(20).
[11] WANG Q, WANG S, ZENG W, et al. Succinylation regulates boar sperm linear motility via reprogramming glucose metabolism [J]. Communications biology, 2025, 8(1): 1319.
[12] ZHANG Z, TAN M, XIE Z, et al. Identification of lysine succinylation as a new post-translational modification [J]. Nature chemical biology, 2011, 7(1): 58-63.
[13] SHEN R, RUAN H, LIN S, et al. Lysine succinylation, the metabolic bridge between cancer and immunity [J]. Genes & diseases, 2023, 10(6): 2470-8.
[14] GUERRERO L, NTZIACHRISTOS P. A succinylation switch to maligancy: SUCLG1, mitochondrial transcription and leukemia [J]. The EMBO journal, 2024, 43(12): 2291-3.
[15] CHEN Q, YANG B, LIU X, et al. Histone acetyltransferases CBP/p300 in tumorigenesis and CBP/p300 inhibitors as promising novel anticancer agents [J]. Theranostics, 2022, 12(11): 4935-48.
[16] WANG Y M, GU M L, MENG F S, et al. Histone acetyltransferase p300/CBP inhibitor C646 blocks the survival and invasion pathways of gastric cancer cell lines [J]. International journal of oncology, 2017, 51(6): 1860-8.
[17] DAS C, ADHIKARI S, BHATTACHARYA A, et al. Epigenetic-Metabolic Interplay in

the DNA Damage Response and Therapeutic Resistance of Breast Cancer [J]. Cancer research, 2023, 83(5): 657-66.
[18] LIU H, TANG Y, SINGH A, et al. RNF20 links the DNA damage response and metabolic rewiring in lung cancer through HIF1α [J]. Nature communications, 2025, 16(1): 4929.
[19] XIAO M, YANG H, XU W, et al. Inhibition of α-KG-dependent histone and DNA demethylases by fumarate and succinate that are accumulated in mutations of FH and SDH tumor suppressors [J]. Genes & development, 2012, 26(12): 1326-38.
[20] SALMINEN A, KAARNIRANTA K, HILTUNEN M, et al. Krebs cycle dysfunction shapes epigenetic landscape of chromatin: novel insights into mitochondrial regulation of aging process [J]. Cellular signalling, 2014, 26(7): 1598-603.
[21] SOUKUPOVA J, MALFETTONE A, HYROŠŠOVá P, et al. Role of the Transforming Growth Factor-β in regulating hepatocellular carcinoma oxidative metabolism [J]. Scientific reports, 2017, 7(1): 12486.
[22] ARNOLD P K, FINLEY L W S. Regulation and function of the mammalian tricarboxylic acid cycle [J]. The Journal of biological chemistry, 2023, 299(2): 102838.
[23] LINDNER A K, TULCHINER G, SEEBER A, et al. Targeting strategies in the treatment of fumarate hydratase deficient renal cell carcinoma [J]. Frontiers in oncology, 2022, 12: 906014.
[24] JANIN M, DAVALOS V, ESTELLER M. Cancer metastasis under the magnifying glass of epigenetics and epitranscriptomics [J]. Cancer metastasis reviews, 2023, 42(4): 1071-112.
[25] FEINBERG A P, KOLDOBSKIY M A, GöNDöR A. Epigenetic modulators, modifiers and mediators in cancer aetiology and progression [J]. Nature reviews Genetics, 2016, 17(5): 284-99.
[26] MULLEN A R, HU Z, SHI X, et al. Oxidation of alpha-ketoglutarate is required for reductive carboxylation in cancer cells with mitochondrial defects [J]. Cell reports, 2014, 7(5): 1679-90.
[27] CHEN Z, NIU K, LI M, et al. GCLC desuccinylation regulated by oxidative stress protects human cancer cells from ferroptosis [J]. Cell death and differentiation, 2025, 32(9): 1679-90.
[28] LI H, ZHANG H, ZHU J, et al. Protein succinylation in tumors-from biology to clinical therapy [J]. International journal of biological macromolecules, 2026, 337(Pt 2): 149489.
[29] LIU J, SUN J, LI C, et al. Post-translational modifications at the crossroads of cancer metabolism and immune regulation: therapeutic opportunities and challenges [J]. International journal of surgery (London, England), 2026, 112(1): 1580-600.
[30] CHEN X, ZHANG J. Understanding Post-Translational Modifications in Porcine Reproductive and Respiratory Syndrome Virus Infection [J]. Veterinary sciences, 2024, 11(12).
[31] SUN Y, HAN B, GE J, et al. CircPSD3 aggravates tumor progression by maintaining TCA cycle and mitochondrial function via regulating SUCLG2 in thyroid carcinoma [J]. Cell death & disease, 2025, 16(1): 590.

[32] HU G, LING C, CHI L, et al. The role of the tryptophan-NAD + pathway in a mouse model of severe malnutrition induced liver dysfunction [J]. Nature communications, 2022, 13(1): 7576.
[33] HAREL M, ORTENBERG R, VARANASI S K, et al. Proteomics of Melanoma Response to Immunotherapy Reveals Mitochondrial Dependence [J]. Cell, 2019, 179(1): 236-50.e18.
[34] AKRAM A W, CHOI D C, CHAE H K, et al. Dihydrogeodin from Fennellia flavipes Modulates Platelet Aggregation via Downregulation of Calcium Signaling, αIIbβ(3) Integrins, MAPK, and PI3K/Akt Pathways [J]. Marine drugs, 2025, 23(5).
[35] NESS M, WENDT K L, PERAMUNA T, et al. Systematic Assessment of the Impact of Targeted Selection Methods and Environment-Mimicking Culture Conditions on Fungal Natural Product Libraries [J]. Journal of natural products, 2026.
[36] PAN Q, YU F, JIN H, et al. eIF3f Mediates SGOC Pathway Reprogramming by Enhancing Deubiquitinating Activity in Colorectal Cancer [J]. Advanced science (Weinheim, Baden-Wurttemberg, Germany), 2023, 10(27): e2300759.
[37] VIJAYANATHAN Y, HO I A W. The Impact of Metabolic Rewiring in Glioblastoma: The Immune Landscape and Therapeutic Strategies [J]. International journal of molecular sciences, 2025, 26(2).
[38] UPADHYAY M, SAMAL J, KANDPAL M, et al. The Warburg effect: insights from the past decade [J]. Pharmacology & therapeutics, 2013, 137(3): 318-30.
[39] ZHANG Y W, SCHöNBERGER K, CABEZAS-WALLSCHEID N. Bidirectional interplay between metabolism and epigenetics in hematopoietic stem cells and leukemia [J]. The EMBO journal, 2023, 42(24): e112348.
[40] DI GREGORIO E, MIOLO G, SAORIN A, et al. From Metabolism to Genetics and Vice Versa: The Rising Role of Oncometabolites in Cancer Development and Therapy [J]. International journal of molecular sciences, 2021, 22(11).
[41] LANZETTI L. Oncometabolites at the crossroads of genetic, epigenetic and ecological alterations in cancer [J]. Cell death and differentiation, 2024, 31(12): 1582-94.
[42] HOU J, SHI M, HONG J, et al. PCAF-mediated acetylation regulates RAD51 dynamic localization on chromatin during HR repair [J]. EMBO reports, 2025, 26(16): 4100-23.
[43] SUN L, WANG X, CHEN L, et al. CPT1A mediates chemoresistance in human hypopharyngeal squamous cell carcinoma via ATG16L1-dependent cellular autophagy [J]. Cell insight, 2023, 2(6): 100127.
[44] MINGUEZ P, PARCA L, DIELLA F, et al. Deciphering a global network of functionally associated post-translational modifications [J]. Molecular systems biology, 2012, 8: 599.
[45] UNRUH D, ZEWDE M, BUSS A, et al. Methylation and transcription patterns are distinct in IDH mutant gliomas compared to other IDH mutant cancers [J]. Scientific reports, 2019, 9(1): 8946.

Figure legends

Fig 1. Succinyl-CoA reprograms DNA damage repair in glioblastoma.

(A) Univariate Cox regression analysis of cancer hallmark pathways (KEGG) and their association with overall survival in GBM patients. **(B)** Correlation between TCA cycle / oxidative phosphorylation activity and homologous recombination deficiency (HRD) scores in GBM datasets. **(C)** Schematic of key enzymes in the tricarboxylic acid (TCA) cycle. **(D)** Quantitative proteomics analysis of differentially expressed proteins between TR and TS GBM groups. **(E)** Untargeted metabolomics profiling identifies differential metabolites in TR *vs*. TS cells. **(F)** Comparison of succinate and α-ketoglutarate (AKG) levels between resistant and sensitive groups. **(G)** Changes in TMZ resistance of GBM cells following treatment with succinate or AKG. **(H)** Representative comet assay images showing effects of succinate or AKG on DNA damage repair, scale bar: 50μm. **(I)** Representative immunofluorescence images of γ-H2AX foci after indicated treatments, scale bar: 20μm. **(J)** Influence of succinate or AKG on intracellular homologous recombination activity. Data are presented as mean ± SEM; * $p < 0.05$, ** $p < 0.01$, ***$p < 0.001$.

Fig 2. Succinyl-CoA upregulates RAD51 succinylation and inhibits its proteasomal degradation.

(A) Correlation between succinyl-CoA (SucciCoA) score and levels of homologous recombination (HR)-related proteins in the Cancer Cell Line Encyclopedia (CCLE). **(B)** Correlation between SucciCoA score and RAD51 protein levels in a GBM proteomic cohort. **(C)** Distribution of differentially expressed proteins in U251 cells after DES treatment. **(D)** Western blot analysis of RAD51 and other HR-related proteins following DES or DMK treatment in U251 cells. **(E)** RAD51 mRNA levels in U251 cells after DES or DMK treatment. **(F)** Detection of endogenous RAD51 succinylation by immunoprecipitation (IP) in U251 cells. **(G)** IP of exogenous Flag-tagged RAD51 followed by immunoblotting with a pan-succinyl-lysine antibody. **(H)** RAD51 succinylation levels in U251 cells treated with DES or DMK. **(I)** RAD51 succinylation in A375 cells after glycine treatment. **(J)** Changes in SucciCoA score in A375 cells following CPI613 or DES treatment. **(K)** RAD51 succinylation in U251 cells after CPI613 or DES treatment. **(L)** Half-life of RAD51 protein in U251 cells following CPI613 or DES treatment. **(M)** Effect of DES or DMK, alone or with MG132 or bafilomycin A1, on

RAD51 levels in LN229 and U251 cells. **(N)** Immunofluorescence showing colocalization of RAD51 with the proteasome subunit PSMA1. Error bars indicate SEM from three independent experiments. Data are presented as mean ± SEM; ns $p > 0.05$, ** $p < 0.01$, ***$p < 0.001$.

Fig 3. Succinylation at RAD51 K156 antagonizes its ubiquitination at K216.

(A) Immunoblot analysis of RAD51 ubiquitination after DES or DMK treatment. **(B)** RAD51 ubiquitination levels in U251 cells versus TR derivatives. **(C)** Protein half-life of RAD51 in U251 and TR cells. **(D)** Flow cytometry analysis of intracellular RAD51 levels after DES treatment. **(E-F)** Western blot of RAD51 ubiquitination after transfection with HA-ubiquitin (wild-type or mutant plasmids). **(G)** Coomassie blue staining of RAD51 immunoprecipitates. **(H)** Mass spectrometry identification of proteins co-precipitated with RAD51. **(I)** RAD51 ubiquitination following overexpression of STUB1 or TRIM23. **(J)** Schematic of the RAD51 K156 succinylation site identified by MS. **(K)** Statistical analysis of peptides containing potential RAD51 succinylation sites from clinical samples. **(L)** RAD51 succinylation in cells expressing site mutants after glycine treatment. **(M)** Degradation of RAD51 mutants after DES or DMK treatment. **(N)** RAD51 ubiquitination after mutation of putative succinylation sites. **(O)** RAD51 ubiquitination in cells expressing ubiquitination site mutants after glycine treatment. Data represent mean ± SEM; * $p < 0.05$, ** $p < 0.01$.

Fig 4. CPT1A-mediated succinylation stabilizes RAD51 protein. (A) Co-immunoprecipitation (Co-IP) assay to identify RAD51-interacting succinyltransferases. **(B)** Molecular docking model of the CPT1A–RAD51 interaction. **(C)** Immunofluorescence (IF) showing the effect of DES/DMK on CPT1A–RAD51 colocalization. **(D)** Endogenous Co-IP of RAD51 and CPT1A. **(E)** Co-IP of exogenous Flag-RAD51 with myc-CPT1A. **(F)** Succinylation of wild-type and mutant RAD51 after CPT1A knockdown. **(G)** Succinylation of wild-type and mutant RAD51 after CPT1A overexpression. **(H)** Effect of CPT1A knockdown or overexpression on RAD51 protein and mRNA levels. **(I)** RAD51 protein half-life after CPT1A overexpression. **(J)** RAD51 ubiquitination following CPT1A overexpression. **(K)** Interaction between RAD51 and CPT1A after CPT1A overexpression. **(L)** Representative

comet assay images after CPT1A knockdown. **(M)** Homologous recombination (HR) capacity after CPT1A knockdown. **(N)** TMZ resistance in U251 cells after CPT1A knockdown. All experiments were repeated three times; error bars denote SEM. Data represent mean ± SEM; ns $p > 0.05$, ***$p < 0.001$

Fig 5. Osthole downregulates RAD51 by inhibiting CPT1A succinyltransferase activity. **(A)** Network pharmacology screen for compounds targeting CPT1A succinyltransferase activity. **(B)** Molecular docking of CPT1A with Osthole, Arctigenin, and Zoomaric Acid. **(C)** Effect of candidate compounds on RAD51 K156 succinylation. **(D)** CPT1A–RAD51 binding after compound treatment (western blot). **(E)** TMZ resistance in U251 cells after drug treatment. **(F)** Comet assay showing DNA damage repair capacity after treatment. **(G)** Immunofluorescence of BrdU and RPA2 foci indicating DNA damage extent. **(H)** Levels of DNA damage markers after combined Ostholend TMZ treatment. **(I)** HR activity score after combination treatment. **(J)** Proliferation capacity after combination treatment. **(K)** *In vivo* imaging of tumor progression in orthotopic GBM models. **(L)** Total fluorescence intensity in different treatment groups. **(M)** Survival analysis of mice receiving combination therapy. **(N)** Immunohistochemical (IHC) detection of DNA damage markers in tumors. **(O)** Quantification of IHC scores for relevant molecules in brain tumor tissues. Data are mean ± SEM; *p < 0.05, **p < 0.01, ***p < 0.001 *vs*. control.

Fig 6. CPT1A-mediated RAD51 K156 succinylation correlates with poor clinical prognosis.

(A) Detection of CPT1A, RAD51, and RAD51 K156su in clinical glioma samples. **(B)** Representative immunofluorescence (IF) images of CPT1A and RAD51 co-expression. **(C)** IF analysis of CPT1A and RAD51 K156su co-localization in tissues. **(D-F)** Correlation between expression levels of CPT1A, RAD51, or RAD51 K156su and patient survival time. **(G)** Correlation analysis of CPT1A and RAD51 protein expression. **(H-J)** Kaplan-Meier survival curves stratified by low or high expression of CPT1A, RAD51, or RAD51 K156su. Log-rank test was used for survival comparison.

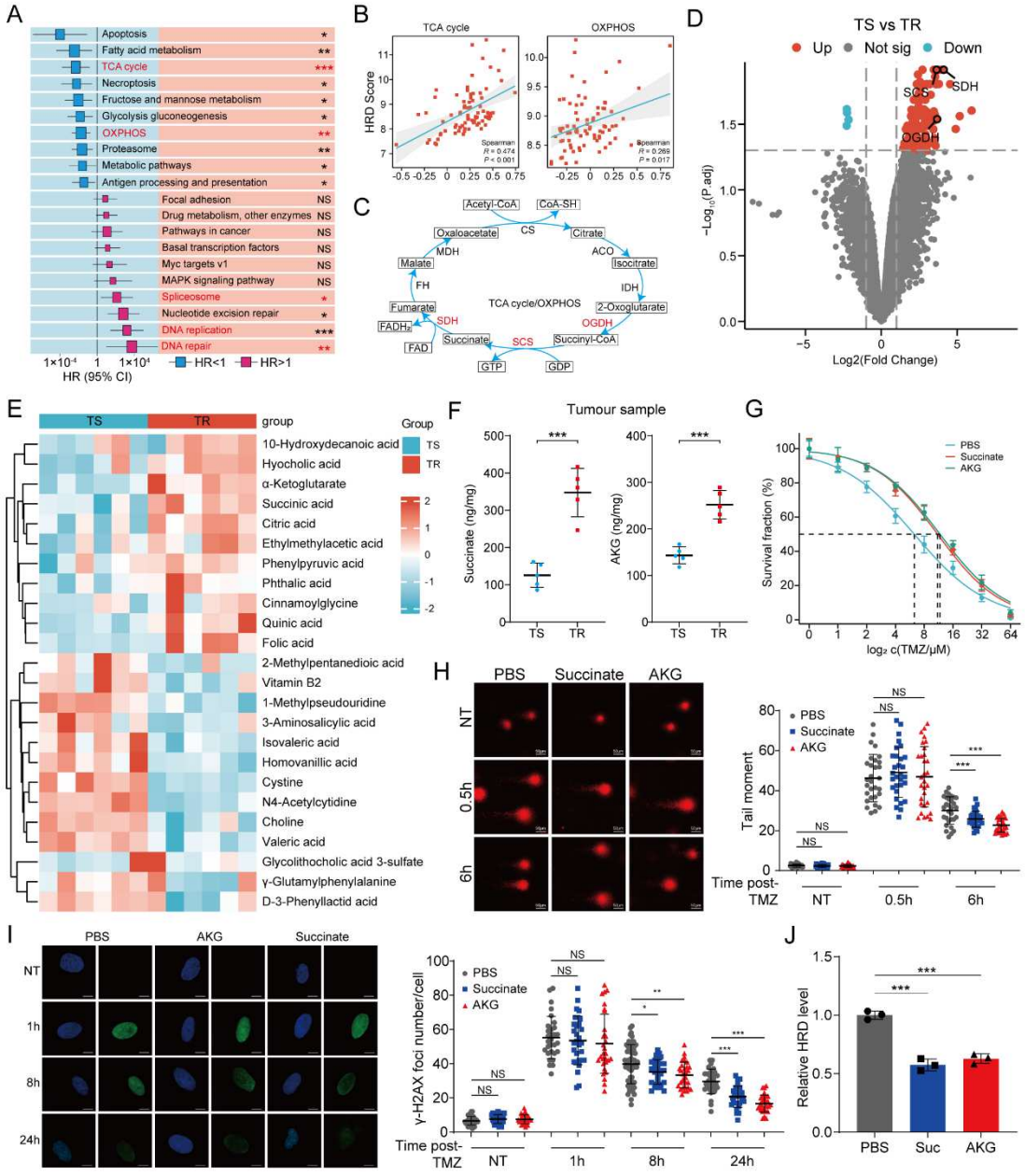
Figure 7. CPT1A and RAD51 Expression Levels Correlate with Chemotherapy Response

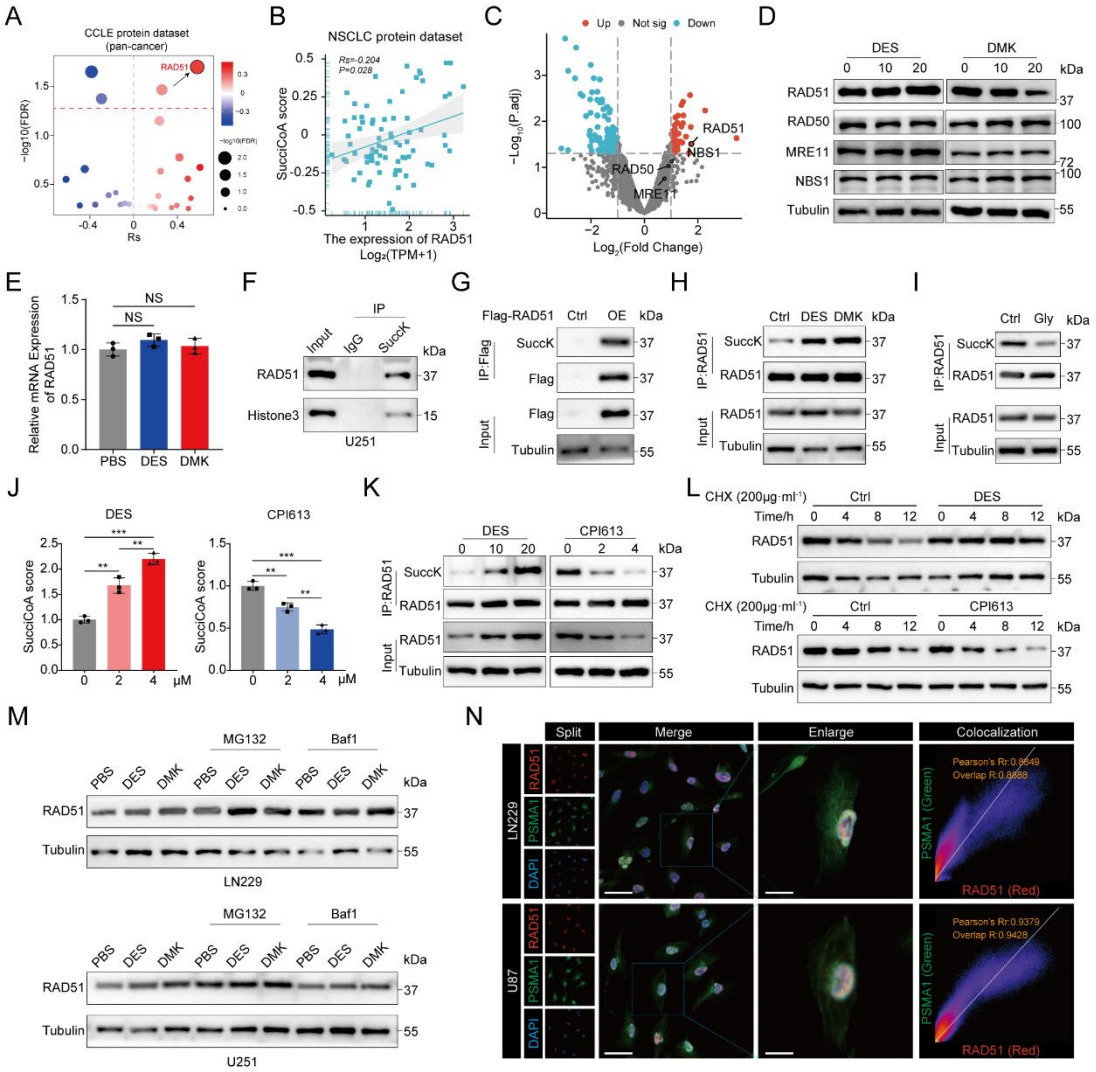
in GBM.

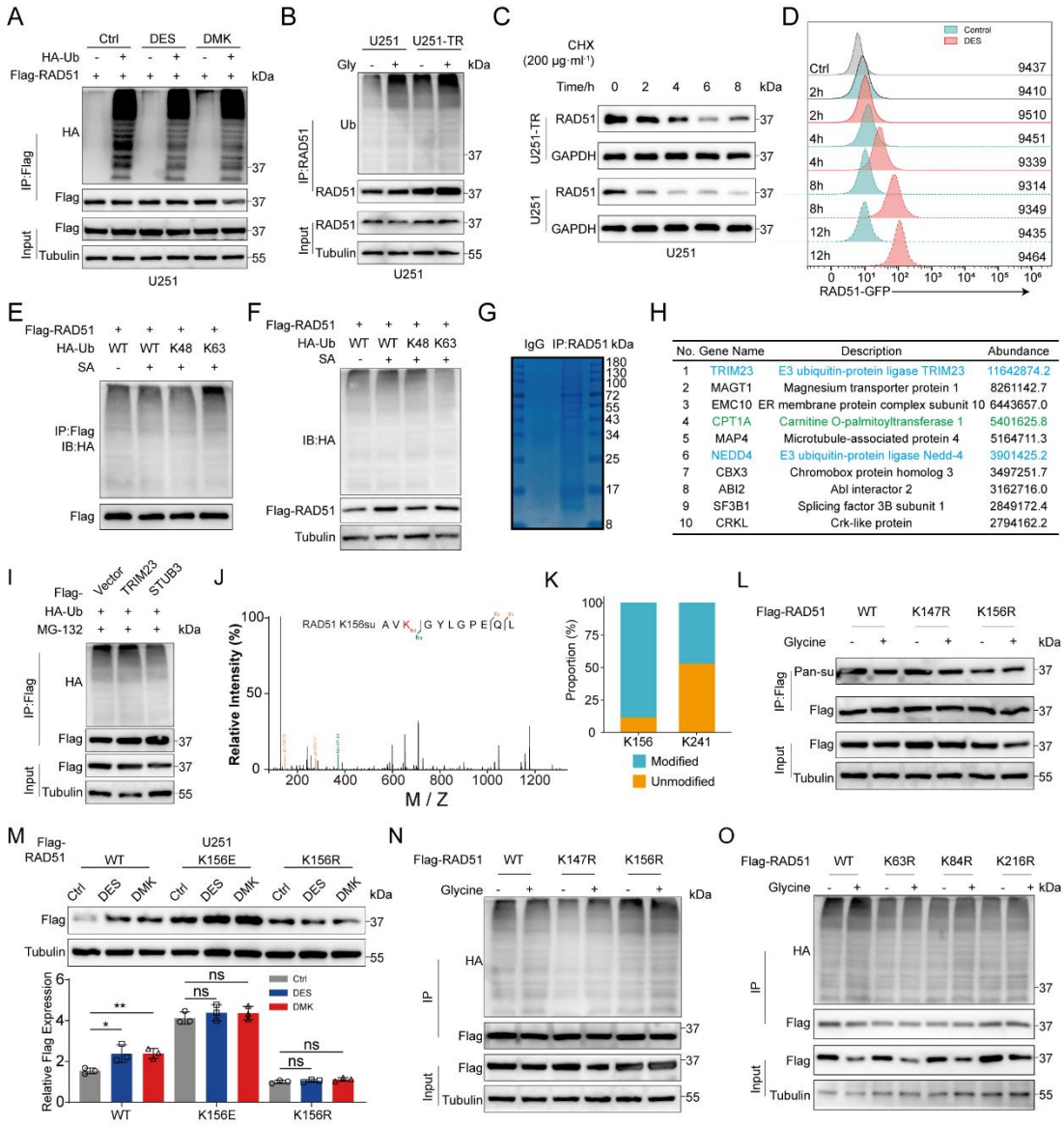
(A) Schematic of the in-house GBM patient cohort. **(B)** Heatmap of clinical characteristics in TS and TR groups. **(C)** Representative IF images of CPT1A and RAD51 co-expression in patient samples. **(D)** Heatmap showing correlation between CPT1A and RAD51 protein levels. **(E)** Violin plots of RAD51 and CPT1A expression in TS *vs*. TR groups. **(F)** Proportion of patients responding to TMZ across expression-based subgroups. **(G)** Kaplan–Meier curves of overall survival in different expression subgroups. **(H)** Summary model: Succinyl-CoA derived from AKG or succinate promotes CPT1A-mediated RAD51 succinylation, which inhibits ubiquitin-proteasome degradation, enhances HR activity, and confers TMZ resistance. Statistical significance was assessed by Student's t-test or ANOVA; *$p < 0.05$, ** $p < 0.01$.

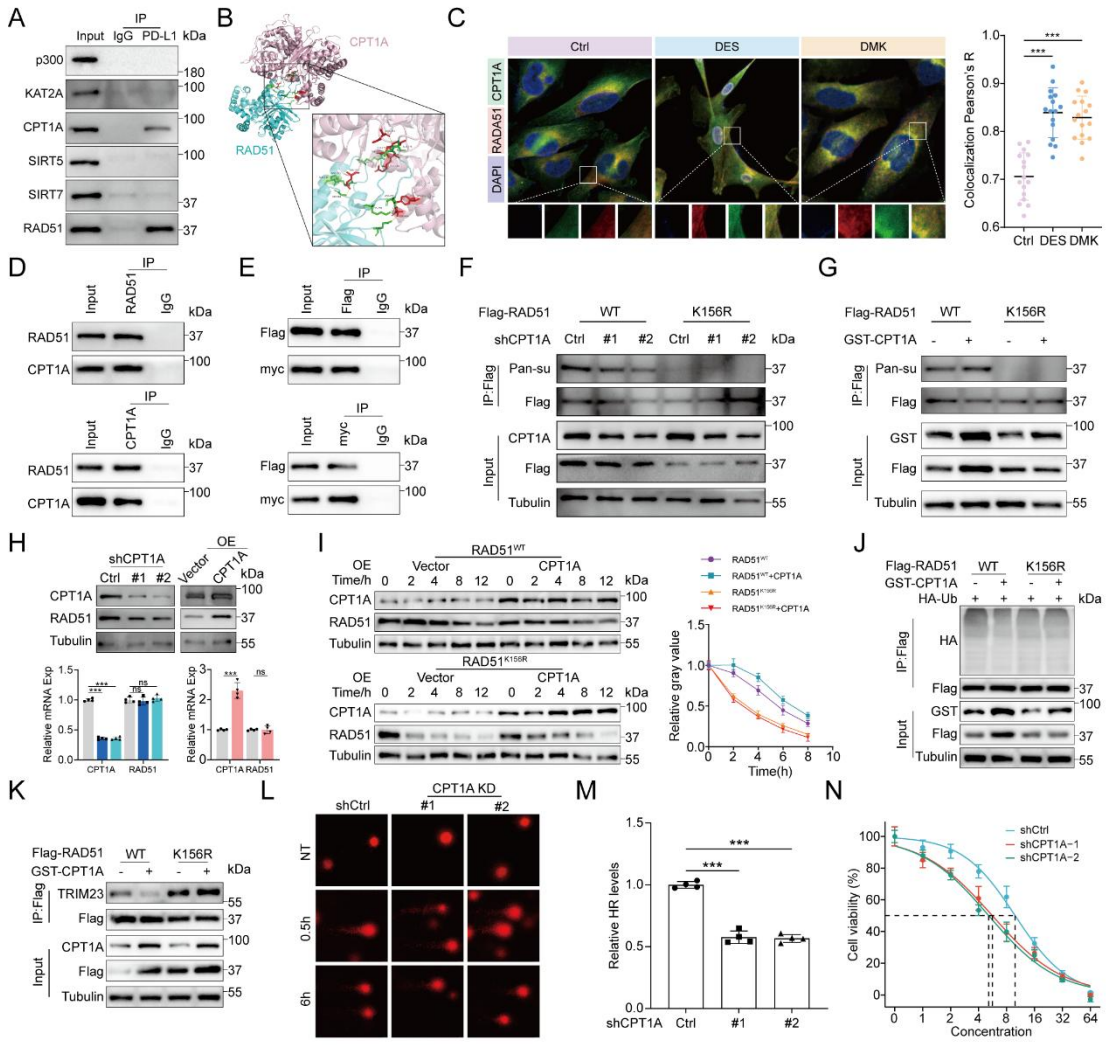
Table 1. The Primer of RT-qPCR.

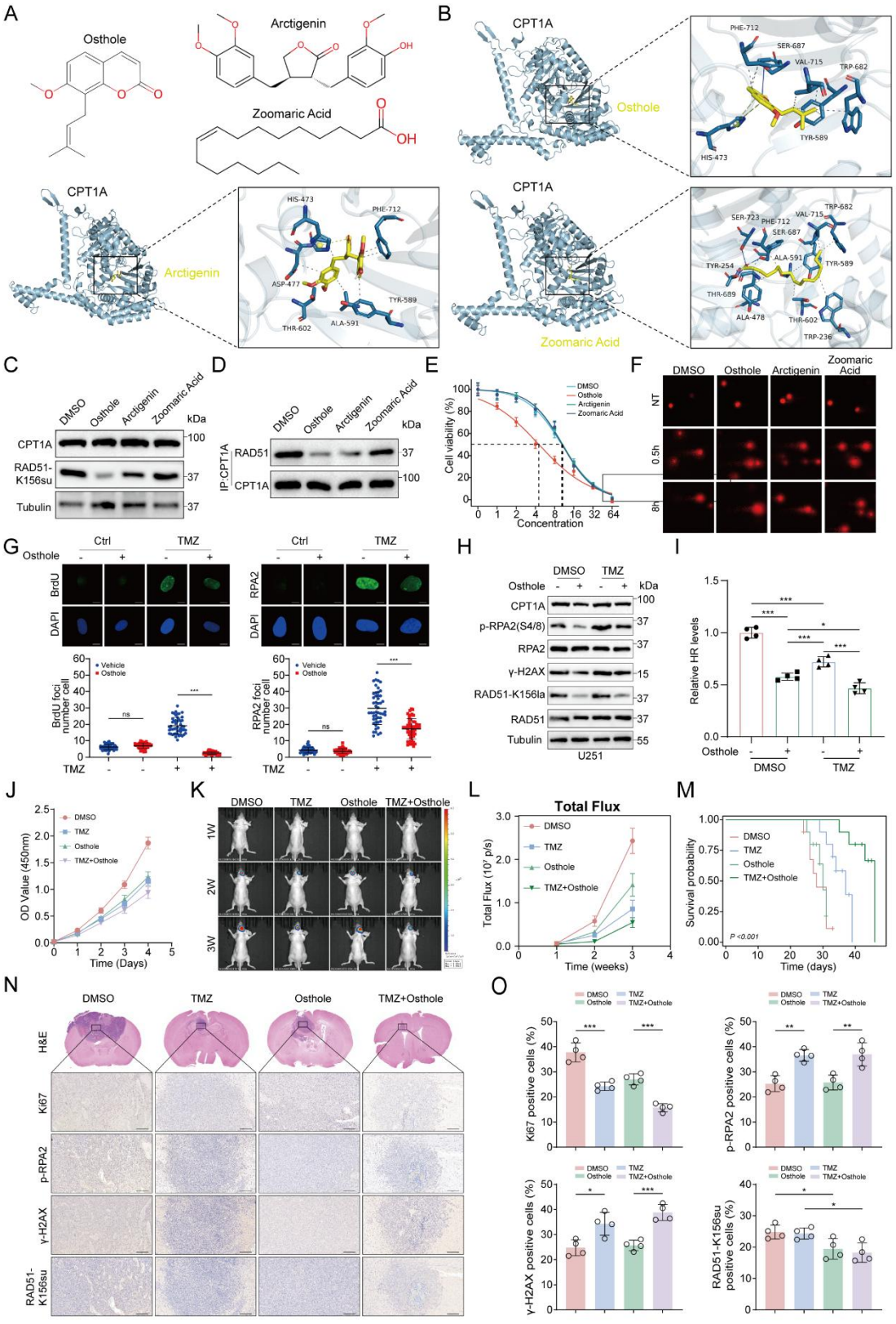
Gene (Homo sapiens)	**Forward（5′-3′）**	**Reverse（5′-3′）**
GAPDH	GGAGTCCACTGGCGTCTTCA	GTCATGAGTCCTTCCACGATACC
RAD51	GAGCTGAAGCTGATGAAGGTG	GGTGGTGGTCTTGGTGATGT
CPT1A	TCCTGCTGAGTGGCTGATGT	GGTGGTGATGGTGATGGTGT

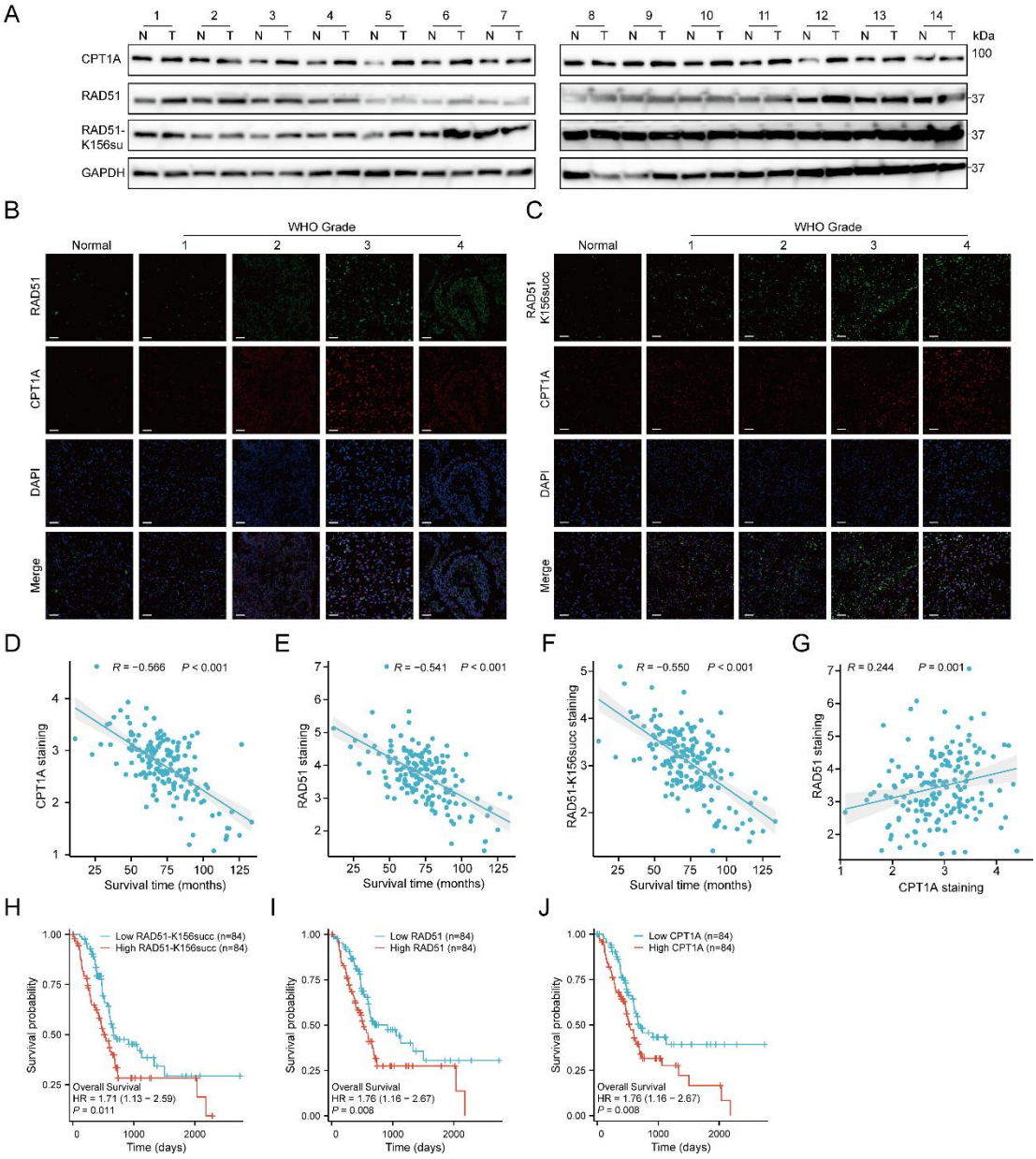

A
Apoptosis *
Fatty acid metabolism **
TCA cycle ***
Necroptosis *
Fructose and mannose metabolism *
Glycolysis gluconeogenesis *
OXPHOS **
Proteasome **
Metabolic pathways *
Antigen processing and presentation *
Focal adhesion NS
Drug metabolism, other enzymes NS
Pathways in cancer NS
Basal transcription factors NS
Myc targets v1 NS
MAPK signaling pathway NS
Spliceosome *
Nucleotide excision repair *
DNA replication ***
DNA repair **
1×10⁻⁴ 1 1×10⁴ HR<1 HR>1
HR (95% CI)
B
TCA cycle
OXPHOS
HRD Score
Spearman R = 0.474 P < 0.001
Spearman R = 0.269 P = 0.017
C
Acetyl-CoA
CoA-SH
CS
Citrate
ACO
Isocitrate
IDH
2-Oxoglutarate
OGDH
Succinyl-CoA
SCS
GTP
GDP
Succinate
SDH
FAD
FADH2
Fumarate
FH
Malate
MDH
Oxaloacetate
TCA cycle/OXPHOS
D
TS vs TR
Up Not sig Down
SCS
SDH
OGDH
−Log10(P adj)
Log2(Fold Change)
E
TS TR
group
Group
TS
TR
10-Hydroxydecanoic acid
Hyocholic acid
α-Ketoglutarate
Succinic acid
Citric acid
Ethylmethylacetic acid
Phenylpyruvic acid
Phthalic acid
Cinnamoylglycine
Quinic acid
Folic acid
2-Methylpentanedioic acid
Vitamin B2
1-Methylpseudouridine
3-Aminosalicylic acid
Isovaleric acid
Homovanillic acid
Cystine
N4-Acetylcytidine
Choline
Valeric acid
Glycolithocholic acid 3-sulfate
γ-Glutamylphenylalanine
D-3-Phenyllactid acid
F
Tumour sample
Succinate (ng/mg)
AKG (ng/mg)
TS TR
G
PBS
Succinate
AKG
Survival fraction (%)
log2 c(TMZ/μM)
H
PBS Succinate AKG
NT
0.5h
6h
Tail moment
Time post-TMZ
NT 0.5h 6h
I
PBS AKG Succinate
NT
1h
8h
24h
γ-H2AX foci number/cell
Time post-TMZ
NT 1h 8h 24h
J
Relative HRD level
PBS Suc AKG

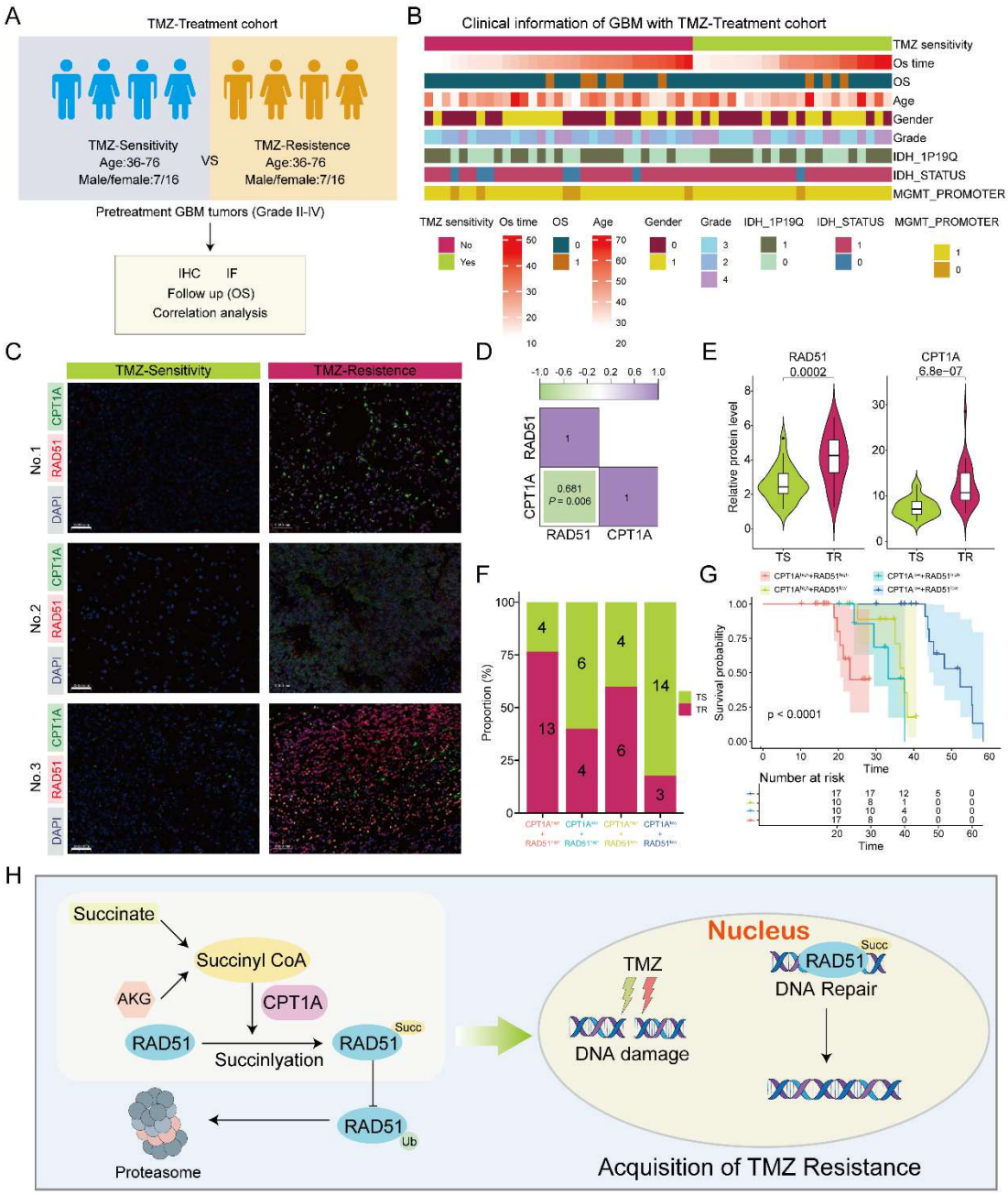

A
CCLE protein dataset
(pan-cancer)
RAD51
−log10(FDR)
Rs
B
NSCLC protein dataset
Rs=-0.204
P=0.028
SucciCoA score
The expression of RAD51
Log2(TPM+1)
C
Up
Not sig
Down
RAD51
NBS1
RAD50
MRE11
−Log10(P.adj)
Log2(Fold Change)
D
DES
DMK
RAD51
RAD50
MRE11
NBS1
Tubulin
kDa
E
NS
Relative mRNA Expression of RAD51
PBS
DES
DMK
F
IP
Input
IgG
SuccK
RAD51
Histone3
U251
G
Flag-RAD51
Ctrl
OE
IP:Flag
SuccK
Flag
Input
Tubulin
H
Ctrl
DES
DMK
IP:RAD51
I
Ctrl
Gly
J
DES
CPI613
SucciCoA score
μM
K
DES
CPI613
L
CHX (200μg·ml⁻¹)
Time/h
M
MG132
Baf1
PBS
DES
DMK
LN229
U251
N
Split
Merge
Enlarge
Colocalization
LN229
U87
RAD51
PSMA1
DAPI
Pearson's Rr:0.9649
Overlap R:0.8828
Pearson's Rr:0.9379
Overlap R:0.9428
PSMA1 (Green)
RAD51 (Red)


A
Ctrl
DES
DMK
HA-Ub
Flag-RAD51
kDa
IP:Flag
HA
Flag
Input
Tubulin
U251
B
U251
U251-TR
Gly
Ub
IP:RAD51
RAD51
Input
Tubulin
U251
C
CHX
(200 μg·ml⁻¹)
Time/h 0 2 4 6 8 kDa
U251-TR
RAD51
GAPDH
U251
D
Control
DES
Ctrl 9437
2h 9410
2h 9510
4h 9451
4h 9339
8h 9314
8h 9349
12h 9435
12h 9464
RAD51-GFP
E
Flag-RAD51
HA-Ub WT WT K48 K63
SA
IP:Flag
IB:HA
Flag
F
Flag-RAD51
HA-Ub WT WT K48 K63
SA
IB:HA
Flag-RAD51
Tubulin
G
IgG IP:RAD51 kDa
180
130
100
72
55
43
34
25
17
8
H
No. Gene Name Description Abundance
1 TRIM23 E3 ubiquitin-protein ligase TRIM23 11642874.2
2 MAGT1 Magnesium transporter protein 1 8261142.7
3 EMC10 ER membrane protein complex subunit 10 6443657.0
4 CPT1A Carnitine O-palmitoyltransferase 1 5401625.8
5 MAP4 Microtubule-associated protein 4 5164711.3
6 NEDD4 E3 ubiquitin-protein ligase Nedd-4 3901425.2
7 CBX3 Chromobox protein homolog 3 3497251.7
8 ABI2 Abl interactor 2 3162716.0
9 SF3B1 Splicing factor 3B subunit 1 2849172.4
10 CRKL Crk-like protein 2794162.2
I
Flag- Vector TRIM23 STUB3
HA-Ub
MG-132
kDa
IP:Flag
HA
Flag
Input
Tubulin
J
RAD51 K156su A V K G Y L G P E Q L
Relative Intensity (%)
M / Z
K
Proportion (%)
K156
K241
Modified
Unmodified
L
Flag-RAD51 WT K147R K156R
Glycine
kDa
IP:Flag
Pan-su
Flag
Input
Tubulin
M
Flag-RAD51
U251
WT
K156E
K156R
Ctrl DES DMK
kDa
Flag
Tubulin
Relative Flag Expression
Ctrl
DES
DMK
ns
**
*
WT
K156E
K156R
N
Flag-RAD51 WT K147R K156R
Glycine
kDa
IP
HA
Flag
Input
Tubulin
O
Flag-RAD51 WT K63R K84R K216R
Glycine
kDa
IP
HA
Flag
Input
Tubulin


A
IP
Input IgG PD-L1 kDa
p300
KAT2A
CPT1A
SIRT5
SIRT7
RAD51
180
100
100
100
37
37
B
CPT1A
RAD51
C
Ctrl
DES
DMK
CPT1A
RADA51
DAPI
Colocalization Pearson's R
Ctrl DES DMK
D
IP
Input RAD51 IgG kDa
RAD51
CPT1A
Input CPT1A IgG kDa
RAD51
CPT1A
E
IP
Input Flag IgG kDa
Flag
myc
Input myc IgG kDa
Flag
myc
F
Flag-RAD51 WT K156R
shCPT1A Ctrl #1 #2 Ctrl #1 #2 kDa
IP:Flag
Pan-su
Flag
Input
CPT1A
Flag
Tubulin
G
Flag-RAD51 WT K156R
GST-CPT1A - + - +
IP:Flag
Pan-su
Flag
Input
GST
Flag
Tubulin
H
shCPT1A
Ctrl #1 #2
OE
Vector CPT1A
kDa
CPT1A
RAD51
Tubulin
Relative mRNA Exp
CPT1A RAD51
I
RAD51WT
OE
Vector CPT1A
Time/h 0 2 4 8 12 0 2 4 8 12 kDa
CPT1A
RAD51
Tubulin
RAD51K156R
Relative gray value
Time(h)
J
Flag-RAD51 WT K156R
GST-CPT1A - + - +
HA-Ub + + + + kDa
IP:Flag
HA
Flag
Input
GST
Flag
Tubulin
K
Flag-RAD51 WT K156R
GST-CPT1A - + - + kDa
IP:Flag
TRIM23
Flag
Input
CPT1A
Flag
Tubulin
L
shCtrl
CPT1A KD
#1 #2
NT
0.5h
6h
M
Relative HR levels
shCPT1A Ctrl #1 #2
N
shCtrl
shCPT1A-1
shCPT1A-2
Cell viability (%)
Concentration


A
Osthole
Arctigenin
Zoomaric Acid
OH
CPT1A
Arctigenin
HIS-473
PHE-712
ASP-477
TYR-589
ALA-591
THR-602
B
CPT1A
Osthole
PHE-712
SER-687
VAL-715
TRP-682
TYR-589
HIS-473
CPT1A
Zoomaric Acid
SER-723
PHE-712
VAL-715
TRP-682
SER-687
ALA-591
TYR-589
TYR-254
THR-689
ALA-478
THR-602
TRP-236
C
DMSO
Osthole
Arctigenin
Zoomaric Acid
kDa
CPT1A
RAD51-K156su
Tubulin
100
37
37
D
DMSO
Osthole
Arctigenin
Zoomaric Acid
kDa
IP:CPT1A
RAD51
CPT1A
37
100
E
DMSO
Osthole
Arctigenin
Zoomaric Acid
Cell viability (%)
Concentration
F
DMSO
Osthole
Arctigenin
Zoomaric Acid
NT
0.5h
8h
G
Osthole
Ctrl
TMZ
BrdU
DAPI
RPA2
BrdU foci number cell
RPA2 foci number cell
Vehicle
Osthole
ns
TMZ
H
DMSO
TMZ
Osthole
kDa
CPT1A
p-RPA2(S4/8)
RPA2
γ-H2AX
RAD51-K156la
RAD51
Tubulin
100
37
37
15
37
37
55
U251
I
Relative HR levels
Osthole
DMSO
TMZ
J
OD Value (450nm)
Time (Days)
DMSO
TMZ
Osthole
TMZ+Osthole
K
DMSO
TMZ
Osthole
TMZ+Osthole
1W
2W
3W
L
Total Flux
Total Flux (10⁷ p/s)
Time (weeks)
M
Survival probability
Time (days)
P <0.001
N
DMSO
TMZ
Osthole
TMZ+Osthole
H&E
Ki67
p-RPA2
γ-H2AX
RAD51-K156su
O
Ki67 positive cells (%)
p-RPA2 positive cells (%)
γ-H2AX positive cells (%)
RAD51-K156su positive cells (%)


A
CPT1A
RAD51
RAD51-K156su
GAPDH
kDa
100
37
37
37
B
C
Normal
WHO Grade
RAD51
CPT1A
DAPI
Merge
RAD51 K156succ
D
E
F
G
R = −0.566 P < 0.001
CPT1A staining
Survival time (months)
R = −0.541 P < 0.001
RAD51 staining
R = −0.550 P < 0.001
RAD51-K156succ staining
R = 0.244 P = 0.001
H
I
J
Low RAD51-K156succ (n=84)
High RAD51-K156succ (n=84)
Survival probability
Overall Survival
HR = 1.71 (1.13 − 2.59)
P = 0.011
Time (days)
Low RAD51 (n=84)
High RAD51 (n=84)
HR = 1.76 (1.16 − 2.67)
P = 0.008
Low CPT1A (n=84)
High CPT1A (n=84)


A
TMZ-Treatment cohort
TMZ-Sensitivity
Age:36-76
Male/female:7/16
VS
TMZ-Resistence
Age:36-76
Male/female:7/16
Pretreatment GBM tumors (Grade II-IV)
IHC IF
Follow up (OS)
Correlation analysis
B
Clinical information of GBM with TMZ-Treatment cohort
TMZ sensitivity
Os time
OS
Age
Gender
Grade
IDH_1P19Q
IDH_STATUS
MGMT_PROMOTER
No
Yes
C
TMZ-Sensitivity
TMZ-Resistence
No.1
No.2
No.3
CPT1A
RAD51
DAPI
D
RAD51
CPT1A
0.681
P = 0.006
E
RAD51
0.0002
CPT1A
6.8e−07
Relative protein level
TS
TR
F
Proportion (%)
TS
TR
G
Survival probability
p < 0.0001
Time
Number at risk
H
Succinate
Succinyl CoA
AKG
CPT1A
RAD51
Succinlyation
Succ
Proteasome
Ub
Nucleus
TMZ
DNA damage
DNA Repair
Acquisition of TMZ Resistance

Supplementary Files

This is a list of supplementary files associated with this preprint. Click to download.

- UncroppedGelsandBlots.docx